scientific reports

Check for updates

OPEN

A combined experimental and modeling approach to elucidate the adsorption mechanism for sustainable water treatment via In$_2$S$_3$-anchored chitosan

Soumya Ranjan Mishra, Prerona Roy, Vishal Gadore & Md. Ahmaruzzaman✉

A novel Chitosan/Indium sulfide (CS/In$_2$S$_3$) nanocomposite was created by co-precipitating Chitosan and InCl$_3$ in solution, resulting in In$_2$S$_3$ agglomeration on the Chitosan matrix with a remarkable pore diameter of 170.384 Å, and characterized it for the physical and chemical properties. Under optimal conditions (pH = 7, time = 60 min, catalyst dosage = 0.24 g L^{-1}, and dye concentration = 100 mg L^{-1}), the synthesized nanocomposite demonstrated remarkable adsorption capabilities for Victoria Blue (VB), attaining a removal efficiency of 90.81%. The Sips adsorption isotherm best matched the adsorption process, which followed pseudo-second-order kinetics. With a rate constant of 6.357 × 10^{-3} g mg^{-1} min^{-1}, the highest adsorption capacity (q$_m$) was found to be 683.34 mg g^{-1}. Statistical physics modeling (SPM) of the adsorption process revealed multi-interaction and multi-molecular adsorption of VB on the CS/In$_2$S$_3$ surface. The nanocomposite demonstrated improved stability and recyclability, indicating the possibility for low-cost, reusable wastewater dye removal adsorbents. These results have the potential to have practical applications in environmental remediation.

Water contamination is a significant environmental hazard that has gained global concern. Both human life and the natural environment have been significantly affected by the same due to the swift decrease in the availability of freshwater resources[1,2]. Various pollutants contaminate water, including organic dyes, phenolic compounds, heavy metal ions, inorganic ions, radioactive wastes, and other pharmaceutical contaminants. Among these, organic dyes are the most hazardous and toxic due to their inherent mutagenicity and carcinogenicity[3,4]. These dyes also degrade very slowly due to their relatively complex and stable structures; hence, they persist and accumulate in the aquatic environment over a long time[5]. Such dyes harm human health and aquatic life by entering the food chain and depleting the hygienic standard of the water it persists in. Therefore, wastewater treatment has become the need of the hour and an essential strategy for a sustainable future[6,7].

Victoria Blue (VB) is a dye that can cause detrimental effects on aquatic ecology and affect human well-being in various ways (Fig. 1). VB is a cationic blue dye (M.W. = 492.5 g/mol) that is biodegradable in nature. It is a brown powder melting at 206 °C, which dissolves in water to form a dark blue solution. It is broadly utilized for dyeing cotton, wool, and silk, as well as for staining and pigmentation of microscopic specimens. Moreover, it acts as a photosensitizer, inducing cytotoxic responses in various mammalian cell linings[8]. It is found to cause eye irritation and, in some cases, permanent opacification on long exposures to human eyes. Other than this, it is also reported to cause fatal diseases such as pneumoconiosis (a lung disease) and skin injuries on prolonged exposure[9]. The decision to investigate this basic dye was motivated by the apparent scarcity of studies on removing this specific VB dye using CS and metal sulfide. Conventional methods for wastewater treatment can be of three types: biological, chemical, and physical. These methods include membrane separation[10], adsorption[11], advanced oxidation[12,13], catalytic ozonation[14], Fenton and electro-Fenton[15], catalytic photodegradation[16–18], electrochemical degradation[19], ultrasonic irradiation[20] and biodegradation[21]. Adsorption has gained widescale popularity due to its easy operations, cost-effectiveness, eco-friendly nature, and broad applicability[22]. Adsorption depends on

Department of Chemistry, National Institute of Technology, Silchar, India. ✉email: mda2002@gmail.com
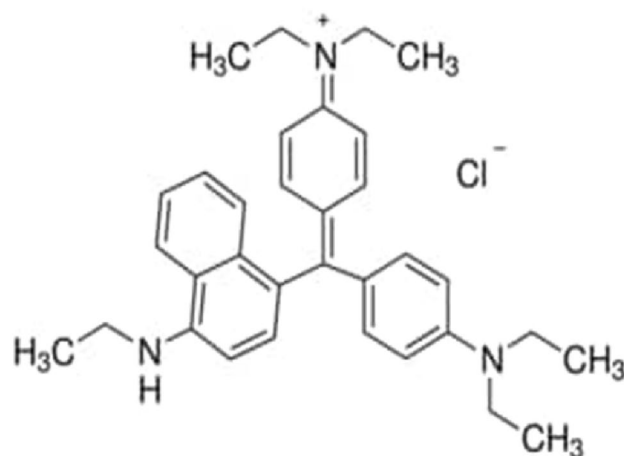
Figure 1. Chemical Structure of VB.

various physicochemical factors, like the surface area of the adsorbent, pH of the solution, operating temperature, and the characteristics of the adsorbate[23]. In this vein, scientists are continuously developing various functional adsorbents for improved elimination of pollutants from an aqueous solution.

Generally, separating the used adsorbent from the treated sample is a typical task. Due to the difficulty in the separation of nanoparticles, several support materials are used to enhance adsorption efficiency. Another reason to use supporting materials is that they prevent the agglomeration of metal sulfide nanoparticles and increase the prepared nanocomposite's surface area, thereby enhancing the adsorption capacity[24]. The properties possessed by an ideal adsorbent include abundant availability of active sites or more considerable surface exposure, high saturation capacity, appropriate pore volume and pore size, convenient accessibility, abundance, selectivity towards the target contaminant, pocket, and environment-friendly nature. Hence, scientists are developing various adsorbents using natural products such as biopolymers as they tend to have higher adsorption capacities and are both environmentally friendly and cost-effective[25]. Biopolymers have been one of the most efficient adsorbent materials worldwide. These have been used effectively in large-scale industrial and large-scale industrial and manufacturing applications for wastewater treatment, food production, drug delivery, biomedical purposes, chemical engineering, and fuel cell production[26]. Among various biopolymers, Chitosan is one of the most inexpensive, non-toxic, available, renewable, biodegradable, and biocompatible amino-polysaccharide[27]. Alkaline deacetylation of the naturally available fiber chitin leads to the creation of chitosan[28]. Perhaps the most prevalent biopolymer in the environment, chitin, is derived from the shells of crustaceans, including prawns, crabs, and lobsters, which are leftovers from the seafood business. Specific properties that make chitosan an efficient adsorbent include its macromolecular structure, cationic, availability, low-cost, eco-friendly nature, and interactive amino and hydroxyl functionalities[29]. It has been described as possessing sturdy inter and intra-molecular hydrogen bonds. However, the strong covalent bonds of chitosan that run along the backbone of the biopolymer chain due to strong hydrogen bonding make it difficult for dye molecules to access its active sites and restrict its solubility, reactivity, and adsorption capability[30]. As an amino polysaccharide, chitosan gains its stable and feasible structure and adsorption efficiency from the existing interactive amino and hydroxyl functionalities[31]. The high amino content of the polymer facilitates various chemical and physical alterations that improve the polymer's adsorption capabilities and adsorption capacity.

Two two-dimensional metal sulfides have recently attracted researchers worldwide for their advanced surface-to-volume ratio, facile synthesis, and tunable surface properties. A wide range of semiconductor nanomaterials has also shown splendid adsorption performances. Various metal sulfides have been synthesized to remove organic contaminants from wastewater. Indium sulfide is a semiconductor with unique thermal, optoelectrical, mechanical, and physical properties[32]. It has a bandgap range from 2.0 eV to 2.4 eV[33]. These are widely used in photodetectors, solar cells, photocatalytic degradation, and biological imaging[34]. Indium sulfide is widely known for its photocatalytic dye removal from wastewater, and its adsorption potential is still a rising topic for worldwide research. Researchers recently fabricated $In_2S_3/g-C_3N_4$ nanocomposite via a hydrothermal method for mercury adsorption[35]. Flower-like β- In_2S_3 was designed to adsorb MB dye[36]. In addition, we have also developed β-In_2S_3/BC for the effective adsorption of methylene blue and malachite green from single and binary systems[37].

This literature aims to fabricate and study the application of CS/In_2S_3 nanocomposite in wastewater treatment by removing VB (λ_{max} = 616 nm) from the contaminated water. The fabricated nanocomposite catalyst has the

advantage of the existing interactive functionalities of the biopolymer, such as the NH_2 and OH groups on the large surface area of the In_2S_3 particles, which enhances the adsorption capacity of the biopolymer towards the target contaminant. The nanocomposite showed appreciable adsorption capacity and removal efficiency towards VB. The developed Chitosan/In_2S_3 nanocomposite showed an exceptionally high q_m of 683.34 mg g^{-1} with an outstanding removal efficiency of 90.81% at room temperature, higher than pristine In_2S_3 nanoparticles. The adsorption procedure obeyed the Sips isotherm model, and the adsorption mechanism was studied using statistical physics modeling (SPM). The interaction between the dye and the adsorbent surface may be used to calculate the experimental adsorption isotherm. The evaluation of isotherm statistics is critical to comprehending the process governing adsorption. The function of the functional groups in the sorption of VB can be examined and tested by fusing SPM calculations with the characterization and adsorption observational findings[38]. Furthermore, data fitting via well-known adsorption isotherm models (such as Langmuir, Sips, Freundlich, and Redlich-Peterson) can result in solid conclusions for maximal adsorption capacity and affinity. However, they do not offer crucial details for elucidating adsorption mechanisms or pertinent information on adsorption dynamics. The mechanism of dye adsorption has been examined using statistical physics models in order to close this knowledge gap. The crystalline composition and topography of the fabricated nanocomposite were extensively studied. This article highlights the fabrication, characterization, application, isotherm, kinetics, thermodynamics, physical modeling, the role of the adsorption parameters and inorganic and organic compounds, water matrices, mechanism, and reusability of the CS/In_2S_3 nanocomposite.

Experimentation
Reagents
Chitosan, Indium chloride tetrahydrate ($InCl_3.4H_2O$), Sodium sulfide nonahydrate ($Na_2S.9H_2O$), Sodium dodecyl sulfate ($NaC_{12}H_{25}SO_4$), HCl, Victoria blue (VB), and ethanol. The aforementioned compounds were obtained from Sigma Aldrich. Since they are of analytical quality, they need not be further purified before usage. Throughout this experiment, de-ionized water is utilized in several procedures.

Although adsorption research is geared toward ecological purposes, the majority of analyses are conducted in de-ionized water. Few studies have investigated the impact of natural water samples on organic contaminants' adsorption activities. An analysis of the influence of various inorganic ions and organic compounds was conducted to gain a better insight into the nanocomposite's effectiveness and remove contaminants from different water samples, such as bottled mineral, tap, and lake water. For this study, packaged bottled mineral water was bought from a nearby shop. Water for the lake was obtained from lakes inside the National Institute of Technology, Silchar, in the Indian state of Assam, which served as the source for the water matrix analysis. Tap water was made available through the neighborhood drinking water systems.

Sample preparation
Fabrication of In_2S_3 nanoparticle
Pristine In_2S_3 nanoparticle was synthesized using the co-precipitation method, as carried out by Kennedy et al.[39]. 2 mmol of Indium chloride tetrahydrate ($InCl_3.4H_2O$) and 0.1 mmol of Sodium dodecyl sulfate ($NaC_{12}H_{25}SO_4$) was taken in a beaker and stirred at 500 rpm for about 30 min at room temperature. After that, 3 mmol of Sodium sulfide nonahydrate ($Na_2S.9H_2O$) solution was introduced dropwise into the above solution, and the mixture was agitated at 1200 rpm for two h at 60 °C. As a result, a bright yellow precipitate was obtained, which was rinsed with de-ionized water and ethanol, and dried at 65 °C until the final product was obtained.

Fabrication of CS/In_2S_3 nanocomposite
The CS/In_2S_3 adsorbent was also produced through the simple co-precipitation technique, following the work of Gadore et al.[40]. Chitosan was added to 72 mL of 1 M HCl solution and agitated at 1000 rpm for 1 h under moderate heat (Solution A). Simultaneously, indium chloride tetrahydrate ($InCl_3.4H_2O$) was dissolved in 50 mL of de-ionized water and mixed at 1000 rpm for 15 min (Solution B). CS and $InCl_3.4H_2O$ were taken in a 1:1 weight ratio. After that, solution B was mixed with solution A, and the resulting solution (Solution C) was heated and agitated at 1200 rpm for 1 h. 1.5 mmol sodium sulfide nonahydrate ($Na_2S.9H_2O$) solution was added dropwise to solution C with constant mixing and moderate heating. The final solution was kept under magnetic stirring for 1 h, and the resulting precipitate was centrifuged, washed with ethanol and de-ionized water, and dried at 65 °C till the final product was obtained.

Characterization of fabricated CS/In_2S_3
Throughout the work, various analytical methods were used to characterize both In_2S_3 and the composite material CS/In_2S_3. X-ray diffraction (XRD) was carried out using Philips X'PERT equipment, Cu-K radiation, and a scanning rate of 2° per minute at room temperature. We also used Transmission electron microscopy (TEM) with a JEOL JEM 2100 apparatus to examine the diffraction patterns of CS/In_2S_3, concentrating on characterizing diffraction ring forms, diameters, and size distribution. SEM and Elemental mapping was carried out on an FEI Quanta FEG 200-High Resolution Scanning Electron Microscope to analyze the surface characteristics, elemental distribution, and composition of the produced nanocomposite. The sample's elemental composition was carefully determined using energy-dispersive X-ray (EDX) analysis. The Brunauer–Emmett–Teller (BET) technique was used to calculate the specific surface area of the materials using the Quantachrome Novae 2200 instrument. Furthermore, an X-ray Photoelectron Spectroscopy (XPS) investigation was performed on the materials using a Thermafischer scientific Nexsa base system to get insight into their chemical composition and bonding states. To record the absorbance spectrum, UV–visible (UV–Vis) spectroscopic data were obtained using a GENESYS 10S UV–visible spectrophotometer with a quartz cuvette with a path length of 1 cm and a wavelength scan speed

of 600 nm per minute. These scientific procedures enabled a complete and exact assessment of the materials under consideration.

Adsorption analysis

The sorption tests were carried out in dark conditions at a temperature of nearly 298 K. Fluctuating dye concentrations and catalyst dosages optimized the adsorption effectiveness of the generated adsorbent. 6–14 mg of the adsorbent were added to a 50 mL mixture containing 100 ppm VB to maximize the catalyst dosage. The mixture that emerged was swirled in the dark for 60 min. 2 mL of the resulting mixture was then transferred to a test tube and centrifuged. The effectiveness of the adsorbent was ascertained by gauging the absorbance of the subsequently separated mixture with a UV–visible spectrophotometer at an λ_{max} of 616 nm. The optimal dye concentration was then determined by introducing the optimized catalyst quantity to a range of VB dye concentrations (100⁻160 mg L⁻¹). The dye concentration and catalyst dosage were optimized to evaluate the adsorption capacity (q_e), contact time, and impact on adsorption due to different organic and inorganic substances and water matrices. In order to analyze the adsorption isotherms again, the optimal dosage of the nanocomposite was added to beakers containing 50 mL of 10–400 mg L⁻¹ VB at a varied temperature of 298–398 K, and the resultant solution was stirred in the dark for 60 min. The following Eqs. (1) and (2) can be utilized to obtain the adsorption capacity and removal efficacy.

$$Efficiency\% = \frac{C_0 - C_t}{C_0} \times 100 \tag{1}$$

$$q_e = \frac{C_0 - C_e}{m} \times V \tag{2}$$

Where V is the total volume of the solution (mL), m represents the mass of the adsorbent or nanocomposite (mg), C_0, C_t, and C_e are the concentrations of the dye solution time at the initial stage, at time t, and equilibrium (mg L⁻¹), and q_e is the maximum adsorption capacity of the nanocomposite (mg g⁻¹).

Statistical physics modeling to elucidate the dye removal mechanism

Organic pollutants like VB can be absorbed by creating one or more adsorption layers on the adsorbent. As a result, two distinct statistical physics models that considered the creation of mono and multiple adsorption layers, which clarified the dye adsorption mechanism, were utilized to fit the investigational isotherm calculations. For the experiment, dye solutions of 10–400 mg L⁻¹. were taken and were adsorbed at temperatures from 298 to 328 K for an equilibrium time. The obtained non-linear curve was fitted to the model to acquire the desired parameters.

Results and discussions

Characterization of the prepared nanocomposite

CS/In₂S₃ nanocomposite was synthesized via an in-situ growth procedure employing the co-precipitation technique. Firstly, Chitosan was dissolved in HCl, followed by indium chloride, adding In³⁺ ions to incorporate into the chitosan matrix. Secondly, the CS/In₂S₃ was precipitated by adding sodium sulfide (Na₂S), forming In₂S₃ on the chitosan matrix. The fabricated nanocomposite was characterized to establish the structure, morphology, composition, and topography.

X-ray diffraction analysis
The structure of the CS/In₂S₃ nanocomposite was first characterized by XRD to determine the phase composition and structural and chemical features of the fabricated nanocomposite. The XRD plot of the fabricated nanomaterial and nanocomposite and the magnified XRD plot of the nanocomposite are displayed in Fig. 2a,b, correspondingly. The XRD plot in Fig. 2a shows one intense and distinct crystalline peak for chitosan polymer at 2θ = 12.19° indexed to the reflection plane (2 2 0). Previous studies revealed the mean intermolecular distance of the crystalline components of chitosan and discovered that intramolecular and intermolecular hydrogen bonds are principally accountable for chitosan's firm crystalline structure[41]. In the XRD plot of pure CS, the amorphous phase of the polymer is represented by two broad peaks centered at 2θ = 55° and 35°[42]. However, in the XRD plot of the nanohybrid, it is observed that the intensity of two broad peaks has remarkably reduced; this might be owed to the interaction between the metal sulfide and Chitosan. Therefore, it can be inferred that the formation of the nanocomposite has relatively reduced the amorphous nature of the biopolymer. The XRD data of In₂S₃, as depicted in Fig. 2a,b, showed numerous intense and distinct Bragg's reflection peaks. The peaks displaying the angle 2θ = 23.39⁰, 27.54⁰, 29.61⁰, 47.72⁰, 55.80⁰, 62.21⁰ and 77.53⁰ can be indexed to the (2 0 0), (2 1 3), (1 0 9), (2 2 12), (4 1 9), (5 1 2) and (6 1 5) reflections of tetragonal In₂S₃ (associated with JCPDS Card No. 73–1366) owning space group I41/amd (141), lattice parameters a = 7.623 Å and c = 32.360 Å[43,44]. It is fascinating to observe that analogous XRD patterns were detected in CS/In₂S₃ (Fig. 2b), indicating that the indium sulfide developed on the surface of Chitosan grew in (2 2 12) and (1 0 9) directions as the relative diffraction peaks of these lattice planes are relatively high[43]. The average size of the crystallite is obtained from Debye–Scherrer's equation (Eq. 3):

$$D = \frac{k\lambda}{\beta \cos \theta} \tag{3}$$
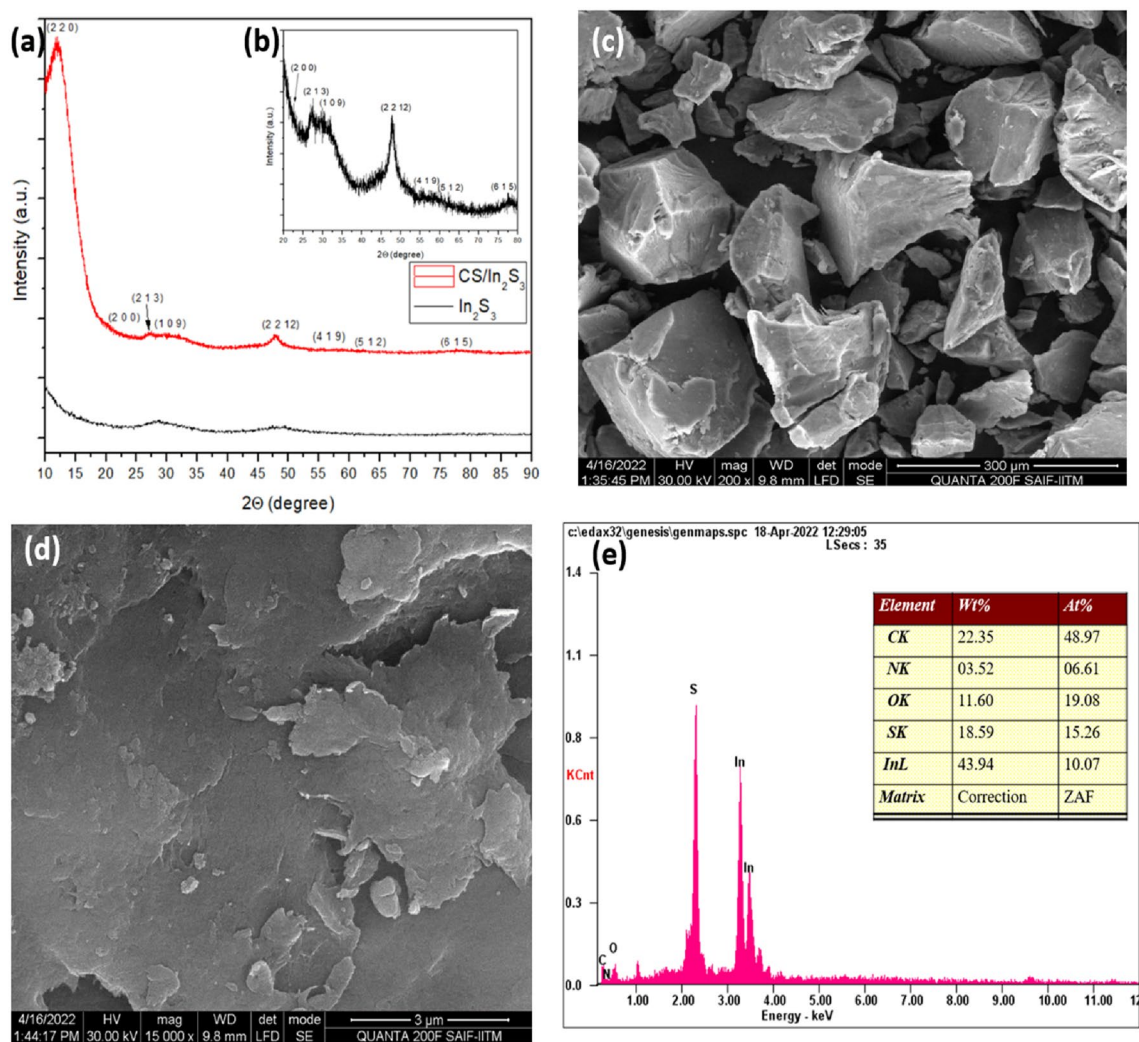
Figure 2. XRD patterns of (**a**) In_2S_3 and CS/In_2S_3; (**b**) magnified peak of CS/In_2S_3; (**c, d**) FE-SEM images, (**e**) EDX analysis of fabricated CS/In_2S_3 (peak table inserted).

where D is the crystallite's size in nanometers (nm), k is its form factor (0.89), λ is the wavelength of CuKα1 radiation (1.54060 Å), is a peak's full width at half maximum (FWHM), and θ is the Bragg's angle of diffraction. The crystallite size D of In_2S_3 is ∼ 9.602 nm.

Scanning electron microscope and EDX analysis
Figure 2c,d demonstrate the FE-SEM images of the synthesized nanocomposite prepared by developing Indium sulfide on the surface of HCl-treated chitosan. The nanocomposites are irregular in shape, and as seen in Fig. 2c, the chitosan surface is relatively uneven. Moreover, some fractures are observed on the surface due to the nanocomposite formation. Thus, it can be concluded that the nanocomposite surface becomes coarse and flake-like due to the grafting of In_2S_3 and chitosan biopolymer[45]. The uneven and porous structure enhanced the adsorption of dye molecules even further[46]. The distribution of elements in the synthesized CS/In_2S_3 was inspected additionally by EDX and portrayed in Fig. 2e. The developed nanocomposite is found to have carbon, oxygen, sulfur, nitrogen, and indium elements in the composite structure, with a weight percentage of 22.35, 11.60, 18.59, 3.52, and 43.94%, respectively. As revealed in Fig. 2e, the atomic percentage suggests that indium and sulfur are present in a 2:3 ratio. Chitosan's persistence in the composite hybrid matrix accounts for the nanocomposite's high atomic percentages of carbon, oxygen, and nitrogen[46].

Transmission electron microscope analysis
The CS/In_2S_3 nanocomposite's structural characteristics were analyzed through a transmission electron microscope (TEM). The TEM pictures in Fig. 3a,b depict the non-uniform dispersion of the nanocomposite. The HR-TEM image (Fig. 3c) revealed the accumulation of the In_2S_3 nanoparticles over the polymeric matrix of CS. The average crystal diameter of CS/In_2S_3 was determined quantitatively using a histogram fitted with Lorentzian function and was calculated to be 26.23 nm (Fig. 3f). The HR-TEM (Fig. 3d) exhibited interplanar lattice spacing of 0.1906 nm and 0.164 nm, which agrees to the (2 2 12) and (4 1 9) planes of In_2S_3. The non-uniform distribution
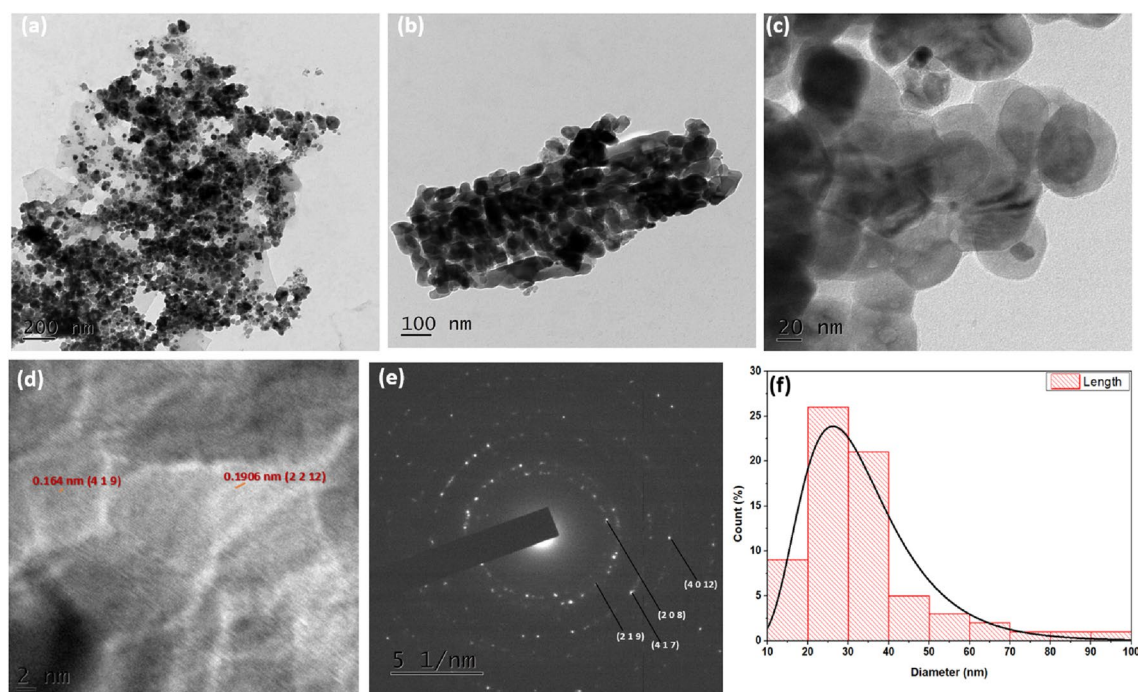
Figure 3. (**a–e**) TEM analysis of the prepared CS/In_2S_3 composite; (**f**) Graph displaying mean particle size of the synthesized CS/In_2S_3 composite.

of intensity along the perimeters of the visible concentric rings depicted in Fig. 3e reveals the polycrystalline nature of the fabricated nanocomposite[47]. Also, as evident from the XRD plot in Fig. 2b, the amorphous nature of the biopolymer is reduced on agglomerating metal sulfides on its surface; hence, its crystalline nature is more predominant[48]. In Fig. 3e, the diameters of four characteristic circles are given as 7.223, 8.331, 11.641, and 12.270 nm, which correspond to the d-spacing of 2.7740, 2.400, 1.718, and 1.556 nm indexed to (2 0 8), (2 1 9), (4 1 7), and (4 0 12) planes of In_2S_3 respectively.

X-ray photoelectron spectroscopy analysis
X-ray photoelectron spectroscopy (XPS) was used to analyze the CS/In_2S_3 nanocomposite's chemical composition. The chemical status and elemental makeup of the CS/In_2S_3 nano adsorbent were revealed by the findings of the XPS survey spectrum, as displayed in Fig. 4a. The survey spectrum showed the distinct peaks of In, S, C, O, and N, with little extra peaks indicating some impurity. Two unique peaks were visible in the HR spectra for In 3d (Fig. 4b), which is due to In $3d_{5/2}$ and In $3d_{3/2}$, correspondingly representing the + 3 oxidation state of In[49]. The crests for S 2p are exhibited in Fig. 4c at energies of 161.32 eV and 162.27 eV, accordingly, which correspond to S's $2p_{1/2}$ and $2p_{3/2}$ sulfide anions and terminal polysulfide[50]. It demonstrates that the component that directly bonds In^{3+} to the chitosan moiety is sulfur. Inferring In_2S_3's existence from this is likewise possible. In the XPS spectrum for carbon C 1 s, as illustrated by Fig. 4d, three distinct peaks are observed at 285.09 eV, 286.29 eV, and 288.51 eV; these show the presence of C–C, C–O–C, and C-O, and C = O and O–C = O bond present in the chitosan matrix correspondingly[51]. The peak for O 1 s (Fig. 4e) shows a distinct rise at 533.1 eV, which depicts a shift from the original value of 530 eV, indicating the formation of the nanohybrid along with presence of C–O–H, C–O–C, and N–C = O bonds in chitosan[51]. Figure 4f illustrates the XPS spectrum for N 1 s, and it shows peaks at 399.35 eV and 399.80 eV, showing the sp^3–C–N bond and N–H bonds present in the base polymer of the nanohybrid, respectively[52].

Elemental mapping and brunauer–emmett–teller analysis
We can infer from Fig. 5 that In_2S_3 nanoparticles are uniformly dispersed over the chitosan surface. The elemental mapping images from Fig. 5a–f show an even dispersal of In, S, C, O, and N in CS/In_2S_3. The CS/In_2S_3 nanocomposite was also characterized by employing the Brunauer–Emmett–Teller (BET) analysis. The nanocomposite's specific surface area was calculated to be 10.0494 m^2/g, while its pore volume and diameter were found to be 0.004470 cm^3/g and 170.384 Å, respectively. The pore diameter size shows the existence of mesopores on the catalyst's surface, inset of Fig. 5g, as it usually ranges between 20 and 500 Å[53]. Thus, the high porosity of the material led to high dye adsorption and increased removal efficiency. Furthermore, the shape of the BJH distribution curve might reveal information on the connectivity of the pores inside the material. A wide distribution of linked holes may allow for improved fluid flow, resulting in remarkable adsorption capability by the manufactured adsorbent. Also, the BET constant c and the q_m were obtained as 17.306906 and 0.2411 cm^3/g at STP. The correlation of the coefficient of BET isotherm is 0.9988473. The N_2 adsorption–desorption curve is depicted in Fig. 5g. We can observe the H1 type of hysteresis curve and type IV BET adsorption isotherm. BET
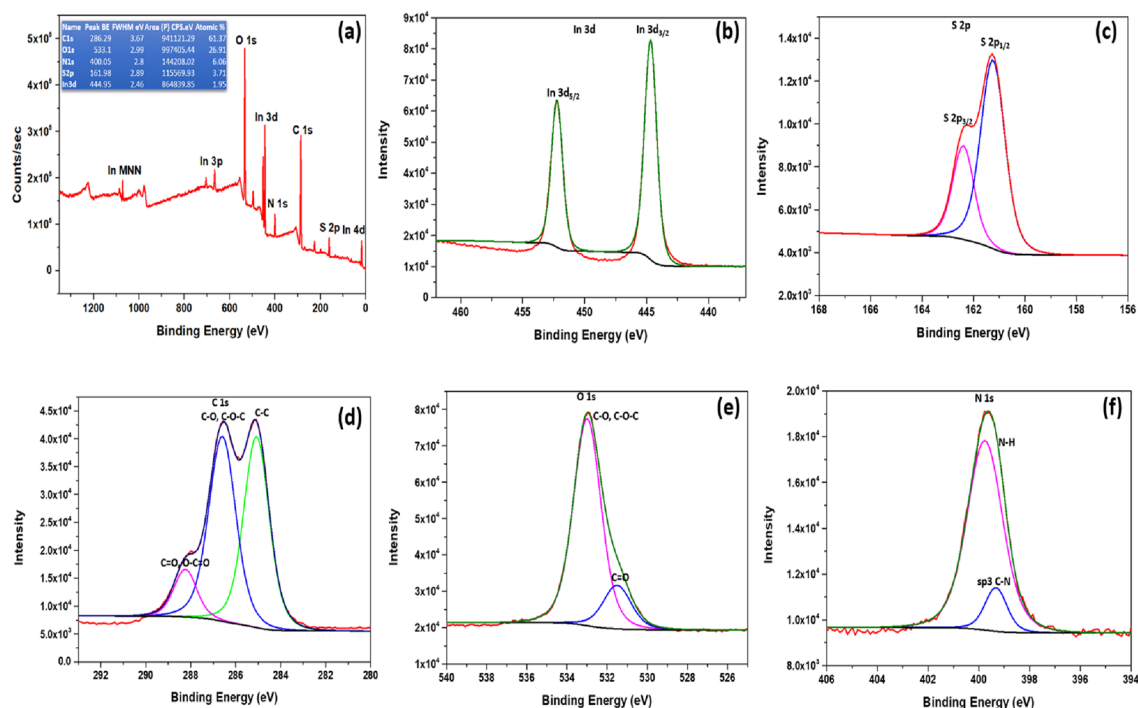
Figure 4. (**a**) Survey spectrum of synthesized CS/In₂S₃ (peak table incorporated). XPS short scan spectrum of (**b**) In3d, (**c**) S2p, (**d**) C1s, (**e**) O1s, (**f**) N1s.

type IV isotherm shows initial monolayer adsorption preceding multilayer adsorption. After the initial monolayer creation, the quantity adsorbed gradually increases in the adsorption isotherm, suggesting the production of multilayers of dye molecules. This is common in porous materials with varying pore diameters[54]. The mesoporous structure of the nanocomposite is further demonstrated by the hysteresis loop[55]. The results suggest that the adsorbent engages in chemisorption because of its reduced BET surface area and pore diameter but significantly higher pore volume.

Adsorption studies of the prepared nanocomposite

VB dye was designated as a typical contaminant to study the adsorption capacity of the prepared CS/In₂S₃ composite. The adsorption isotherm, kinetics, and impact of catalyst doses, dye concentrations, and contact time were studied. As adsorption is temperature-dependent, the influence of temperature upon the removal of the model pollutant was investigated as well, and the thermodynamic variables were calculated. For the appraisal of the adsorbent, the consequence of multiple variables, such as the proportion of inorganic ions and organic compounds and the effect of different water matrices on the adsorption capacity of the prepared adsorbent, in addition to its reusability, was investigated.

Effect of catalyst dosage and dye concentration

The amount of solid nanocomposite is critical to determine the removal percentage of the VB dye. 100 ppm of dye was taken, varying the catalyst dose to 6–14 mg (0.12 g L⁻¹–0.28 g L⁻¹) at room temperature, and was kept for 60 min in the dark. It was found that the 12 and 14 mg doses of the fabricated nanocomposite showed the highest removal percentage of about 90.81% (Fig. 6a). However, the optimum amount is considered to be 12 mg as it displayed an adsorption capacity (q_t) of 279.32 mg L⁻¹. In contrast, the 14 mg catalyst exhibited a q_t of 226.28 mg L⁻¹. Furthermore, a specific mass of adsorbent can only adsorb a certain amount of the solute, making the starting concentration of the adsorbate crucial[56]. The batch adsorption was led to study the removal of VB dye, varying its concentration from 100 to 160 ppm, keeping the catalyst dose constant at 12 mg. The studies revealed that 100 ppm dye concentration showed the highest removal percentage of 90.81%, as shown in Fig. 6b. Therefore, for further studies, such as the influence of contact time, water matrix, the role of organic and inorganic compounds, and reusability, the optimized catalyst dose of 12 mg and dye concentration of 100 ppm was considered.

Effect of pH

This study looked at how pH affected the adsorption of VB onto a composite made of chitosan and In₂S₃. This thorough investigation involves altering pH values between 3 and 11. It was interesting to see that the results showed that the adsorption effectiveness of VB had a definite pH-dependent trend, with the best removal efficiency attained at pH 7, reaching an astounding 90.81% (Fig. 6c). The electrostatic interactions and surface charge characteristics of the CS/In₂S₃ composite material are responsible for this observed trend. The material's surface may have a positive charge under more acidic (lower pH) conditions, encouraging electrostatic interaction with the negatively charged VB molecules[57]. The surface, however, becomes less positively charged as the pH
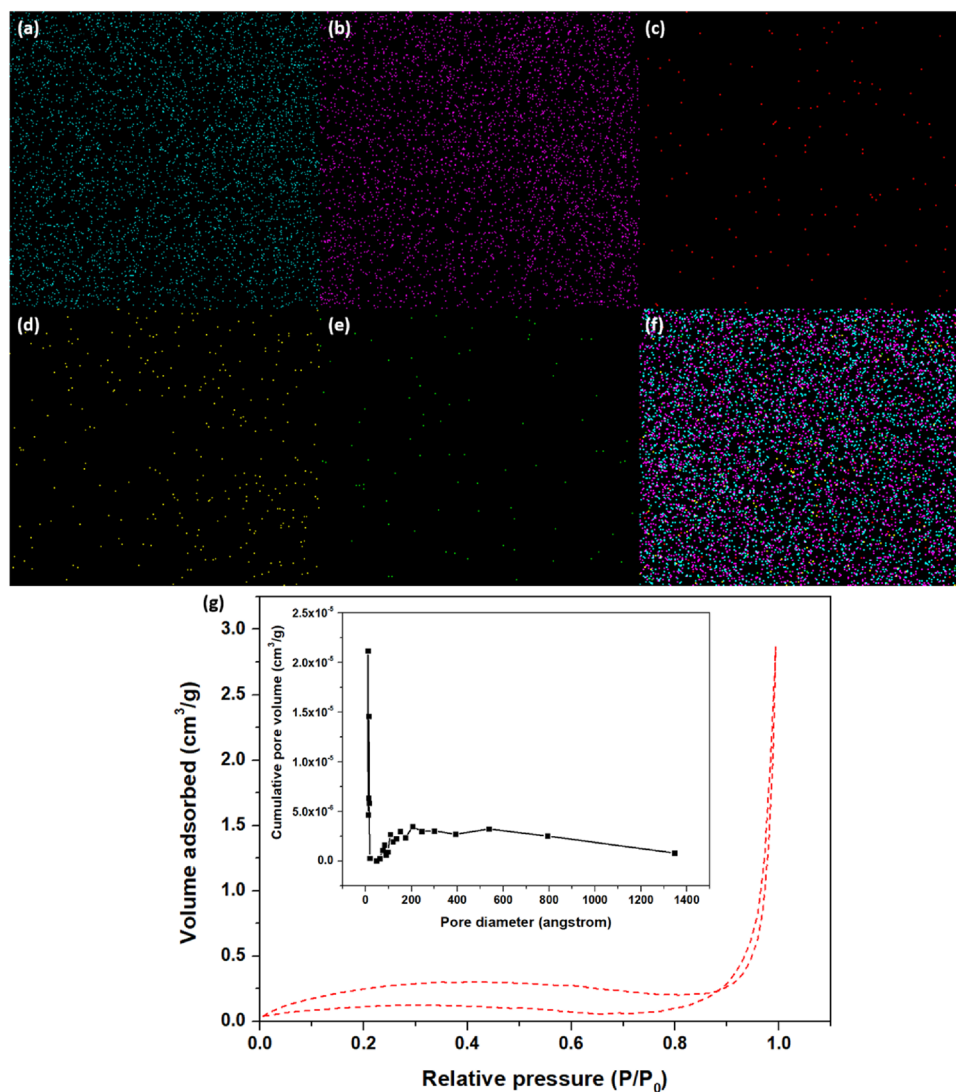
Figure 5. Elemental mapping images of (**a**) Indium, (**b**) sulfur, (**c**) Carbon, (**d**) Oxygen, (**e**) Nitrogen, and (**f**) overall elements for CS/In$_2$S$_3$ nanocomposite; (**g**) N$_2$ adsorption–desorption curve for BET analysis and BJH pore distribution curve (fitted inside).

rises, potentially lowering the adsorption capability. The best removal effectiveness is likely achieved at a pH of 7, which strikes a balance between advantageous electrostatic interactions and changes in the charge state of the VB molecule[58]. These findings have significant significance for maximizing the usage of this composite material in water treatment applications and offer insightful information about the pH-dependent adsorption behavior of VB on CS/In$_2$S$_3$.
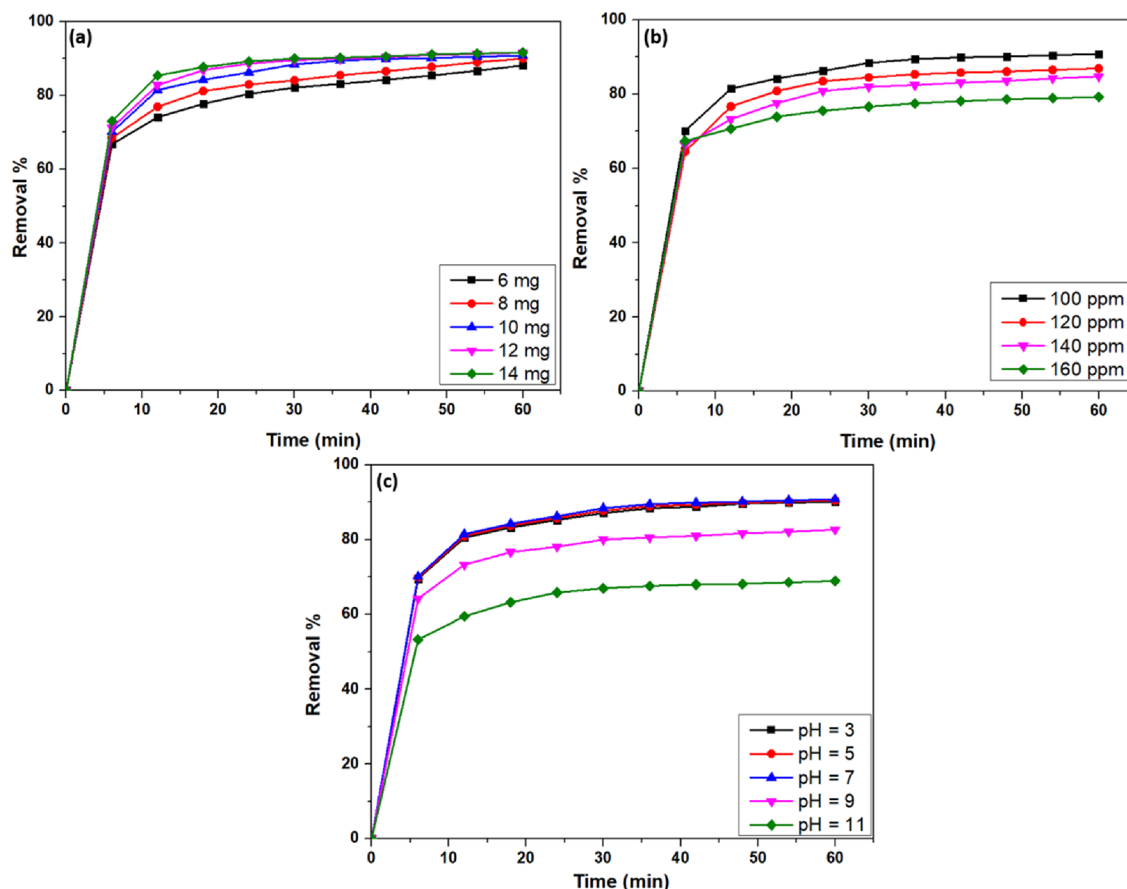
Effect of contact time
Essentially, this research aims to find the optimal environment for maximal adsorption by considering the contact duration between the liquid and solid[59]. The decrease in absorbance due to the decline in concentration is illustrated in Fig. 7a. The VB dye adsorption vs. contact time for a fixed amount of 12 mg of adsorbent demonstrates identical sudden rises at initial times before plateauing, as illustrated in Fig. 7b.

Adsorption isotherm
Equilibrium isotherms define how dye molecules interact with the adsorbent and determine the maximal adsorption capacity (q_m)[60]. The q_m of the fabricated adsorbent can be predicted by analyzing isotherm data, which constitutes one of the critical variables needed for designing adsorption systems[61]. The isotherm evaluations were conducted with variable initial concentrations of VB (10–400 mg L^{-1}) at 298–328 K and 12 mg of the fabricated nanocomposite. Langmuir[62], Freundlich[63], Sips[64], and Redlich-Peterson[65] isotherm models (Fig. 8) were prepared, and it was inferred that the adsorption of VB obeyed the Sips isotherm model, which had the highest correlation coefficient (R^2) of 0.9931, as demonstrated in Table 1. The sips isotherm model is a widely used adsorption model and is considered to be a combination of Langmuir and Freundlich isotherms. The q_m of the fabricated CS/In$_2$S$_3$

Figure 6. Removal percentage due to (**a**) variable catalyst dosage, (**b**) variable dye concentration, and (**c**) variable pH.
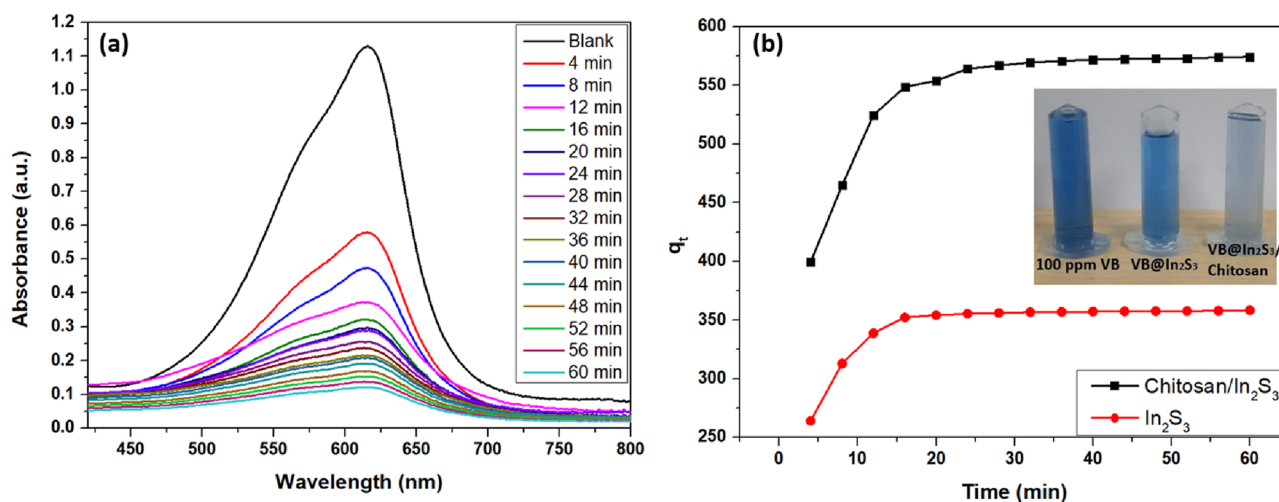
Figure 7. (**a**) Role of contact time on the adsorption of VB; (**b**) Influence on q_t with increasing time.

nanocomposite for VB was found to be 683.34 mg g^{-1} with a Sips constant of 0.0982 L mg^{-1}. Both the monolayer and multilayer adsorption approaches follow the adsorption procedure. Values for 1/n (known as heterogeneity factor) in sips isotherm, near zero, indicate heterogeneous adsorbents, whereas values nearer to or 1.0 suggest the substance with relatively homogenous binding sites. 1/n value near 1 indicates the shifting of the isotherm to the Langmuir model; however, in this case, the values remain close to 0.5 at nearly all temperatures, indicating the co-existence of the monolayer and multi-layer adsorption process. Moreover, this inference was also backed by the BET adsorption–desorption curve, which followed type II adsorption that indicated monolayer adsorption
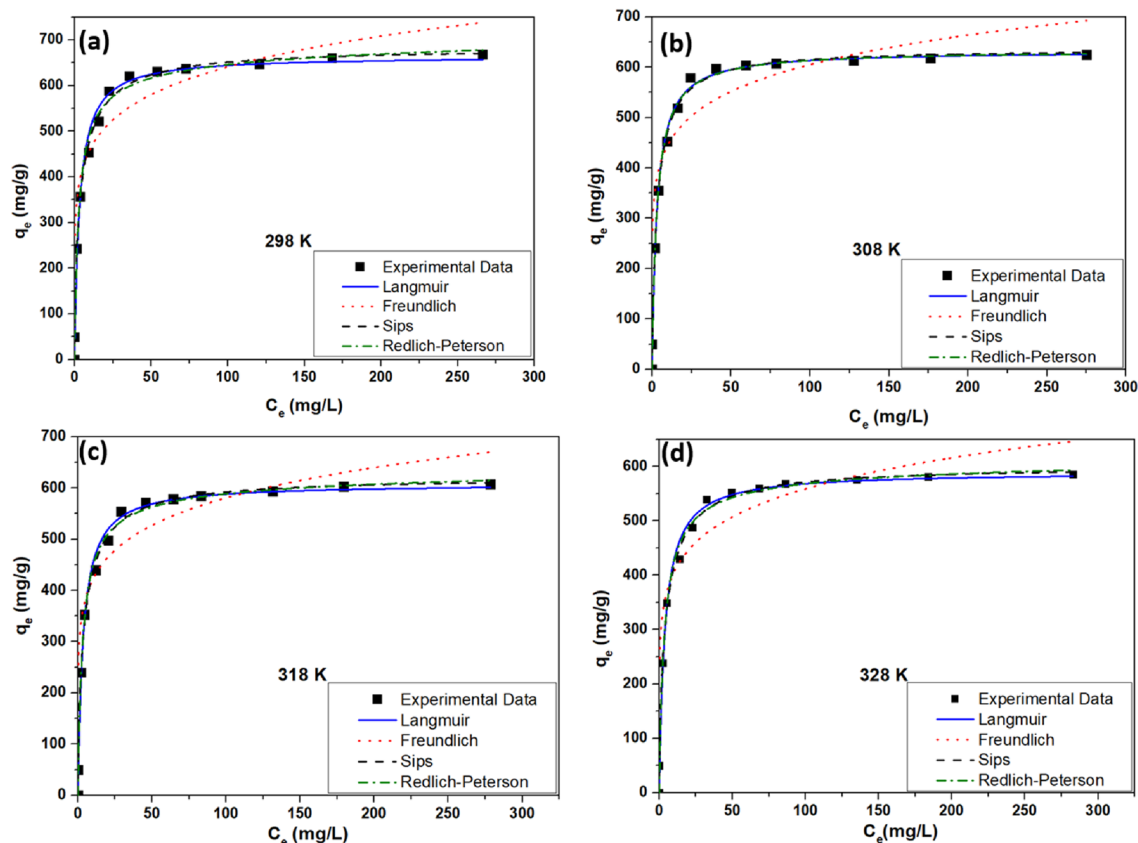
Figure 8. Adsorption isotherm models at varying temperatures.

Isotherm Models	Equations	Parameters	Temperature (Kelvin)			
			298 K	308 K	318 K	328 K
Langmuir	$q_e = \frac{q_m^L b C_e}{1 + b C_e}$	q_m b R^2	664.66 0.3141 0.9855	632.69 0.3173 0.9929	608.48 0.2871 0.9906	598.71 0.2634 0.9904
Freundlich	$q_e = K_F C_e^{1/n}$	K_F $1/n$ R^2	330.18 0.144 0.8227	327.52 0.133 0.7675	305.44 0.1395 0.8151	293.85 0.1396 0.8117
Sips	$q_e = \frac{q_m^s (K_S C_e)^{1/n}}{1 + (K_S C_e)^{1/n}}$	q_m K_s $1/n$ R^2	683.34 0.2982 0.4931 0.9934	637.31 0.2060 0.7445 0.9933	620.82 0.110 0.5451 0.9922	600.72 0.107 0.562 0.9913
Redlich-Peterson	$q_e = \frac{A_{RP} C_e}{1 + B_{RP} C_e^g}$	A_{RP} B_{RP} G R^2	257.12 0.4515 0.9670 0.9901	202.32 0.3226 0.9984 0.9922	201.47 0.3711 0.9759 0.9912	175.75 0.3301 0.9786 0.9904

**Table 1.** Comparison of various parameters by different isotherms.

followed by multilayer adsorption. Table 2 displays that the prepared nanocomposite exhibited a higher q_m for VB than the formerly testified research works.

Adsorption kinetics
Adsorption efficiency depends on a fast reaction rate, a short contact time, and a significant adsorption capacity. The adsorption kinetics of VB by prepared CS/In$_2$S$_3$ nanocomposite was conducted using pseudo-first-order (PFO)[66], PSO[67], and Elovich kinetic models[68], as shown in Fig. 9. The studies found that the adsorption followed PSO kinetics with a rate constant is 6.89×10^{-4} g mg^{-1} min^{-1} as it exhibited the maximum correlation coefficient (R^2) of 0.999 (Table 3). This result indicates that the PSO kinetics fits the sorption behavior of the synthesized nanocomposite towards VB more than the PFO and Elovich models. The PSO model inferred chemisorption of the VB dye, which is backed by the isotherm studies as it obeyed the Sips isotherm model.

Adsorbent	Adsorbate	Adsorption Capacity (q_e) mg g^{-1}	References
Gellan gum/Arginine-bentonite	VB	322.58	[69]
Nanoporous calcined MCM-41 silica	VB	192.3	[70]
Incense stick ash	VB	105.57	[71]
Flower-shaped ZnO	VB	163	[72]
Carbon/Ba/alginate	VB	0.93	[73]
Fe$_2$O$_3$-activated Bakelite	VB	52.63	[74]
Low-cost activated carbon	VB	0.874	[75]
CS/In$_2$S$_3$	VB	683.34	This Work

Table 2. Comparison of several adsorbents utilized to investigate VB adsorption from aqueous solution.
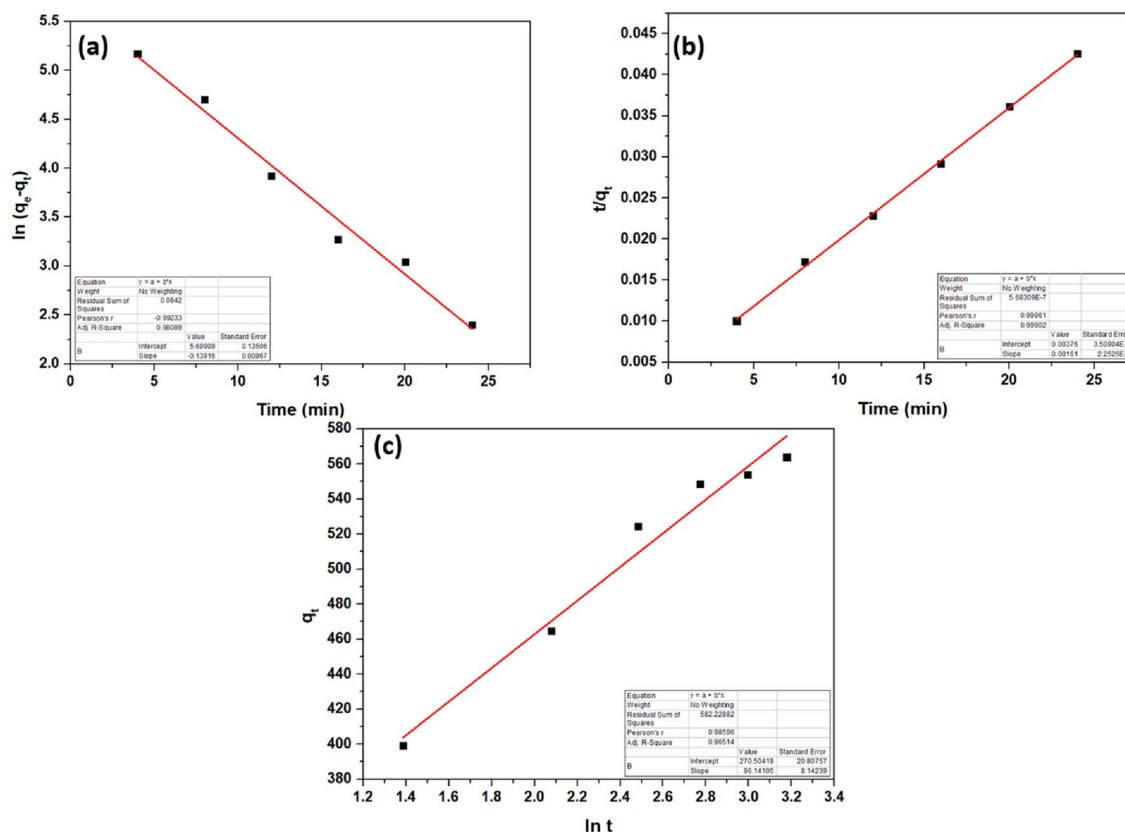
Figure 9. Plots showing (**a**) PFO, (**b**) PSO, and (**c**) Elovich kinetic models.

Kinetic model	Linear equation	Correlation coefficient (R^2)
PFO	$\ln(q_e - q_t) = \ln q_e - k_1 t$	0.9809
PSO	$\frac{t}{q_t} = \frac{1}{k_2 q_e^2} + \frac{1}{q_e} t$	0.999
Elovich	$q_t = \frac{1}{\alpha} \ln(\alpha\beta) + \frac{1}{\alpha} \ln t$	0.9651

Table 3. Fitting of kinetic models.

Adsorption thermodynamics

Thermodynamic factors comprising Gibb's free energy (G°), enthalpy (H°), and entropy (ΔS°) are utilized for estimating the spontaneity level in a sorption technique because the decrease in G°, which has to be -ve for significant sorption to take place, indicates the degree of spontaneity[1,76]. Mathematically, G° and change in Gibbs free energy (ΔG°) are given in Eqs. (4) and (5), respectively.

$$G^0 = -RT \ln K_{ad} \qquad (4)$$

$$\Delta G^0 = \Delta H^0 - T\Delta S^0 \tag{5}$$

where ΔH° and ΔS° are changes in enthalpy and entropy, respectively, and R, T, and K_{ad} are the gas constants, reaction temperature, and adsorption equilibrium constant. Additionally, K_{ad} is equivalent to C_{ad}/C_e, where C_e (mg L^{-1}) is the equilibrium solute concentration and C_{ad} (mg L^{-1}) is the concentration of the adsorbed solute[77]. Combining Eqs. (4) and (5), Vant Hoff's equation is obtained in Eq. (6).

$$\ln K_{ad} = -\frac{\Delta H^0}{RT} + \frac{\Delta S^0}{R} \tag{6}$$

Plotting ln K_{ad} vs. 1/T yields the thermodynamic parameters for adsorption, as seen in Fig. 10a, and ΔH° and ΔS° are determined from the slope and intercept, correspondingly (Table 4). 10 mg of the composite was mixed with 100 ppm VB dye concentration and agitated for 60 min by varying temperature from 298 to 328 K. The obtained ΔH^0 value is negative, which signifies exothermic adsorption, and the enthalpy value is −44.313 kJ mol^{-1}. Negative ΔG^0 values at all temperatures reflect the adsorption process's spontaneity and feasibility, and negative ΔS^0 correlates to a reduction in the degree of freedom of the adsorbed substance[78]. Similar results were obtained by Thamer et al.[79], where the negative ΔG^0 value indicated spontaneous crystal violet adsorption on the ZVNi-NiO@Gr surface. Moreover, because desorption rises with temperature, as illustrated in Fig. 10b, the amount of
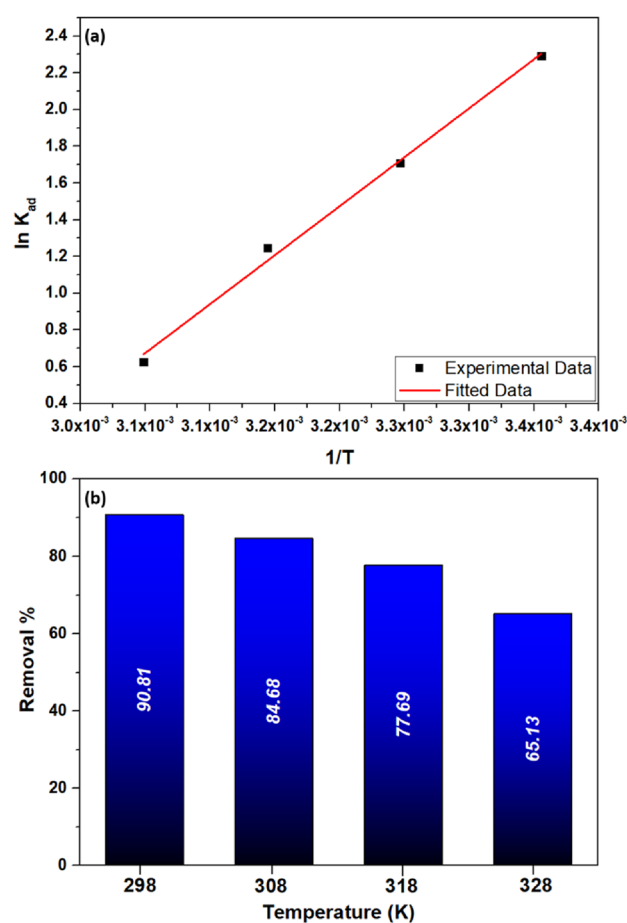
Figure 10. (**a**) Vant Hoff's plot for the removal of VB dye (**b**) Role of temperature on the adsorption of VB.

Temperature (K)	ΔG^0 (kJ mol^{-1})	ΔH^0 (kJ mol^{-1})	ΔS^0 (J K^{-1} mol$^-$)
298	−5.673		
308	−4.376	−44.313	−129.53
318	−3.296		
328	−1.701		

Table 4. Thermodynamic variable at various temperatures.

VB adsorption reduces. Due to the weakening of bonds between the vicinal molecules and the active adsorbent, when the temperature rises, the adsorption may decrease.
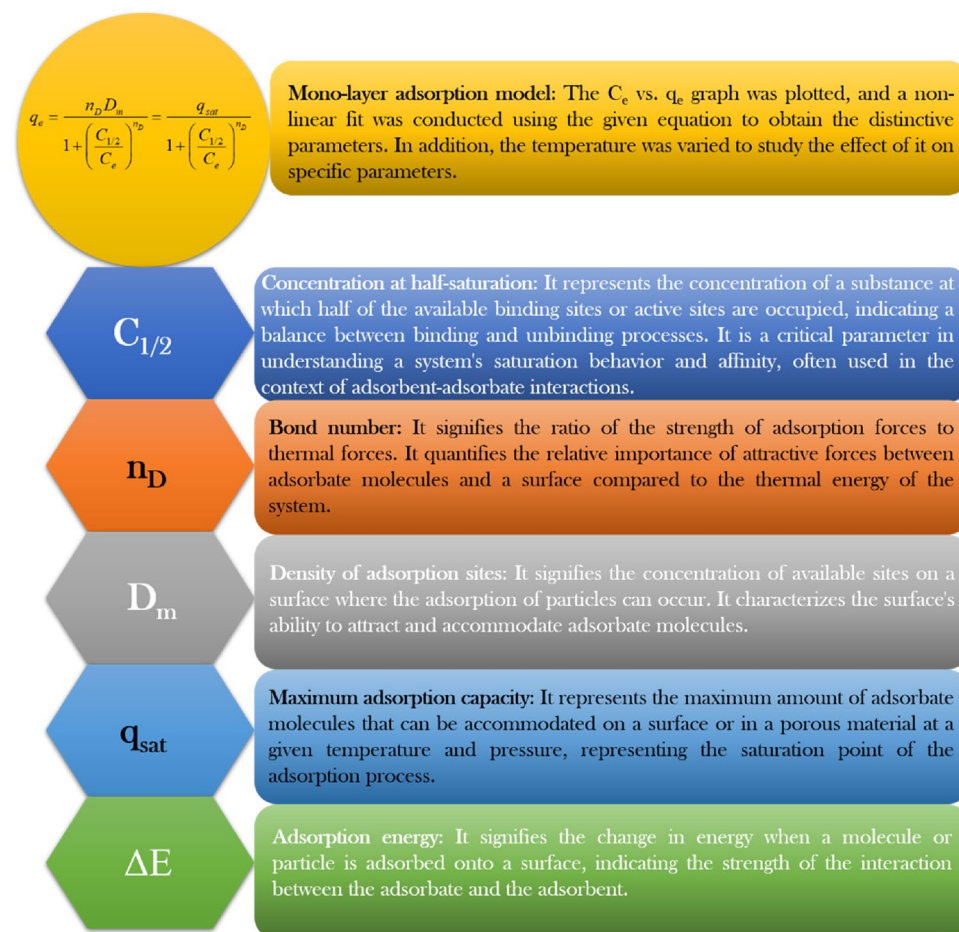
Statistical physics modeling
SPM was employed to analyze the adsorption mechanism and confirm the inference from isotherm studies and BET analysis. The modeling equations help to comprehend the adsorption of VB on CS/In_2S_3 using various parameters. Furthermore, the change in adsorption temperature also played a vital role, which can be confirmed through these modeling. Scheme 1 illustrates SPM analysis, highlighting the calculations and significance of each term. The expression for monolayer adsorption is shown below (Eq. 7)[80]; in this case, all the molecules have single adsorption energy[81].

$$q_e = \frac{n_D D_m}{1 + \left(\frac{C_{1/2}}{C_e}\right)^{n_D}} = \frac{q_{sat}}{1 + \left(\frac{C_{1/2}}{C_e}\right)^{n_D}} \tag{7}$$

This adsorption model has three variables. $C_{1/2}$ is the concentration at half-saturation during adsorption, D_m is the density of adsorption sites, and n_D refers to the amount of VB molecules attached to specific adsorption sites. In this model, the active sites in CS/In_2S_3 were occupied entirely, forming a saturation point. The expression $q_{sat} = n_D * D_m$ refers to adsorption capacity at saturation point.

The expression for the double-layer adsorption model (Eq. 8) assumed that the adsorption of VB molecules on CS/In_2S_3 involved interaction between adsorbate and adsorbent and between the dye molecules[82].

$$q_e = n_D D_m \frac{\left(\frac{C_e}{C_1}\right)^{n_D} + 2\left(\frac{C_e}{C_2}\right)^{2n_D}}{1 + \left(\frac{C_e}{C_1}\right)^{n_D} + \left(\frac{C_e}{C_2}\right)^{2n_D}} \tag{8}$$

Mono-layer adsorption model: The C_e vs. q_e graph was plotted, and a non-linear fit was conducted using the given equation to obtain the distinctive parameters. In addition, the temperature was varied to study the effect of it on specific parameters.

$C_{1/2}$ — **Concentration at half-saturation:** It represents the concentration of a substance at which half of the available binding sites or active sites are occupied, indicating a balance between binding and unbinding processes. It is a critical parameter in understanding a system's saturation behavior and affinity, often used in the context of adsorbent-adsorbate interactions.

n_D — **Bond number:** It signifies the ratio of the strength of adsorption forces to thermal forces. It quantifies the relative importance of attractive forces between adsorbate molecules and a surface compared to the thermal energy of the system.

D_m — **Density of adsorption sites:** It signifies the concentration of available sites on a surface where the adsorption of particles can occur. It characterizes the surface's ability to attract and accommodate adsorbate molecules.

q_{sat} — **Maximum adsorption capacity:** It represents the maximum amount of adsorbate molecules that can be accommodated on a surface or in a porous material at a given temperature and pressure, representing the saturation point of the adsorption process.

ΔE — **Adsorption energy:** It signifies the change in energy when a molecule or particle is adsorbed onto a surface, indicating the strength of the interaction between the adsorbate and the adsorbent.

**Scheme 1.** Significance of the terms obtained from SPM.

At half-saturation, C_1 represents the concentration at which the initial layer forms, whereas C_2 signifies the concentration during the second layer formation. Moreover, the saturated adsorption capacity is denoted as $q_{sat0} = 2 \cdot n_D{}^*D_m$.

In both the monolayer and double-layer adsorption models, the fitting results indicated a high degree of agreement with the investigational statistics, as the R^2 values were close to 1. Nevertheless, this coefficient may not serve as the sole criteria for deciding on a model for determining VB's adsorption on CS/In$_2$S$_3$. The parameters obtained from the monolayer model were more practical and realistic compared to the double-layer model. So, to further investigate the dye's adsorption mechanism on the fabricated nanocomposite, the statistical physics monolayer model was studied, as revealed in Fig. 11a. The fitted variables are discussed in Table 5.

Bonded number of VB molecules (n_D)

The parameter n_D helps to interpret the steric hindrance by giving a theoretical concept for elucidation of the adsorption mechanism of VB on CS/In$_2$S$_3$[83]. Additionally, it highlights how much VB molecules have accumulated in the aqueous solution and how much of them have been adsorbed[84]. The adsorption parameter analyzes the adsorption orientation and is described using the following conditions:

The fact that the VB molecules link to mainly two sites of adsorption on CS/In$_2$S$_3$ and exhibit a pure parallel orientation indicates that the molecules of VB engage in a multi-interaction adsorption mode, according to condition I, where $n_D < 0.5$.
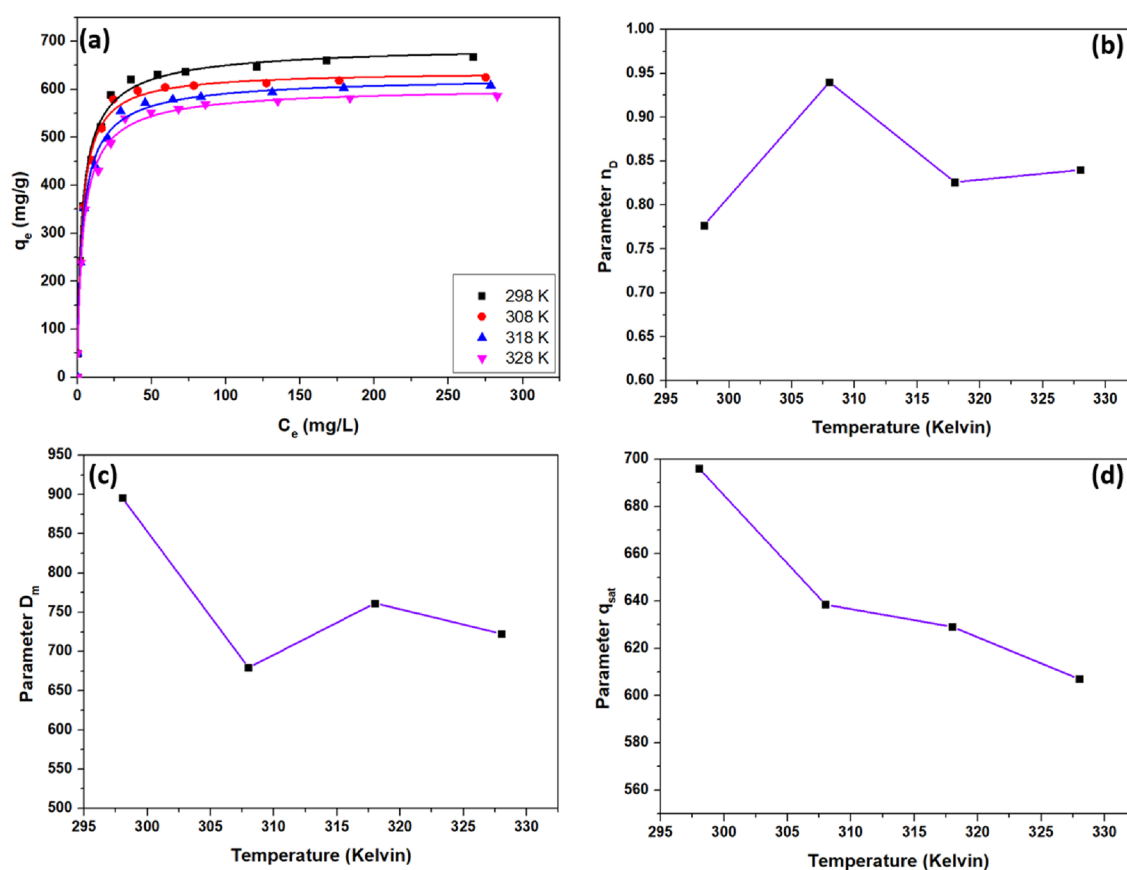
Figure 11. (**a**) Adsorption isotherm of VB on CS/In$_2$S$_3$ and their fitting to statistical physics model; Effect of temperatures on parameters (**b**) n_D, (**c**) D_m, and (**d**) q_{sat} for VB adsorption interpreted from the SPM.

Temperature (K)	n_D	D_m (mg g^{-1})	q_{sat} (mg g^{-1})	$C_{1/2}$ (mg L^{-1})	ΔE (kJ mol^{-1})	R^2
298	0.777	896.03	696.19	3.36	−23.804	0.9921
308	0.94	679.26	638.50	3.15	−24.768	0.9924
318	0.826	761.58	629.06	3.58	−25.234	0.9919
328	0.840	722.61	606.99	3.88	−25.808	0.9917

Table 5. Adjusted parameters of the SPM for adsorption of VB on CS/In$_2$S$_3$.

Condition II, where, $n_D > 1$, implies a multi-molecular adsorption process in which the VB dye molecules seek an active adsorption points and exhibit only non-parallel interactions.

The VB particles are implied to be sorbed in hybrid orientations, i.e., exhibiting mutually parallel and non-parallel interactions, by Condition III where $0.5 < n_D < 1$.

According to the fitting parameters of the physical statistical method, as shown in Table 5, the adsorption of VB molecules followed a hybrid orientation, i.e., it obeyed both parallel and non-parallel interactions. It showcased multi-interaction and multi-molecular adsorption mechanisms as the n_D parameter values ranged from 0.777 to 0.94. The adsorption of AR1 dye on amphoteric adsorbent coating was reported by Azha et al.[85], and the n_D parameters were found to be in the range of 0.52 to 0.83. It was inferred that the adsorption followed a multi-anchorage mechanism, similar to the present work. Furthermore, The fraction of parallel and non-parallel interaction during adsorption can be found by using a simple Eq. 9;

$$n_D = x + (1 - x) \times 0.5 \tag{9}$$

Here, the n_D parameter value is obtained while fitting the SPM; x represents the fraction of non-parallel orientation, and 1-x represents the fraction of parallel orientation. At 298 K, the n_D parameter was found to be 0.777, and the obtained x value was 0.554, which implied that CS/In_2S_3 sorbed 55.4% of VB molecules through non-parallel interaction, whereas 44.6% of VB were adsorbed by parallel orientation. This result also coincides with the inference from isothermal studies and BET analysis. As the temperature increases, the n_D parameter values lie around 0.82 to 1. Temperature change has a frail impact on the molecule accumulation and succeeding anchorage on the adsorption site, as evidenced by this slight variation in the n_D trend (Fig. 11b)[86]. This inference overlaps with the q_m obtained from the Sips isotherm, as no significant decrease was observed.

Density of adsorption sites present in CS/In_2S_3 (D_m)
Figure 11c illustrates the disparity trend of parameter D_m with temperature for VB adsorption on CS/In_2S_3. According to the figure and Table 5, parameter D_m has a different variation trend with temperature than parameter n_D, i.e., parameter D_m increases with temperature, while parameter n_D decreases, and vice-versa. The anchoring number ($n_D' = 1/n_D$) is known to be contrary to parameter n_D, and reducing n_D induces a rise in n_D', increasing adsorption density[87]. Additionally, the volume of operative adsorption sites on the adsorbent reduces as parameter n_D rises due to a reduced distance between adsorption sites on CS/In_2S_3[88]. In comparison to the work done by Sellaoui et al.[89], the adsorption of VB on CS/In_2S_3 showed exothermic adsorption, while their research group inferred endothermic adsorption of nicotinamide and propranolol on magnetic-activated carbon. This led to the opposite trend in the D_m parameter as the initial decrease was attributed to the water adsorption, and a further increase was credited to the freely moving dye molecules due to the temperature rise[89].

Maximum adsorption capacity at saturation (q_{sat})
The quantity of dye an adsorbent can adsorb at a saturated adsorption site is measured by its saturation adsorption capacity. The results in Table 5 indicate that VB has a very high saturation adsorption capacity. This conclusion can be attributed, among other things, to the size of the VB chemical structure, which affects the dye molecules' rate of agility, and the potential for a specific functional group interaction between dyes and adsorbents, which improves adsorption efficacy[37]. As demonstrated in Fig. 11d, as the temperature rises, the saturation adsorption capacity decreases, similar to data obtained in the thermodynamics analysis. This inference indicates that the adsorption mechanism follows the exothermic process. A similar hypothesis was postulated by Wang et al.[90], where the adsorption of rhodamine B, congo red, and naproxen decreased with increased temperature.

Adsorption energy analysis
Calculating and studying adsorption energy can help understand how VB dye molecules attach to CS/In_2S_3. Table 5 displays the correlation findings for adsorption energy. The absorption energy was calculated via the concentration at half-saturation, as shown in Eq. 10.

$$C_{1/2} = C_s e^{\frac{\Delta E}{RT}} \tag{10}$$

The half-saturation concentration is based on the dye's water solubility (Cs) and adsorption energy[83]. The SPM was used to fit experimental data, and the adsorption energies that define the interaction between VB molecules and the CS/In_2S_3 adsorbent surface were determined. As calculated, the negative adsorption energy values solidify the inference of exothermic adsorption processes. Moreover, the adsorption energies were close to the borderline value of 23 kJ mol^{-1}, which signified the existence of both chemical and physical adsorption mechanisms. The chemical process was driven by covalent and ionic bonding, whereas the physical process was carried out due to Vander Waals interaction and hydrogen bonding[91]. From this, we can conclude that the SPM agrees with the isotherm studies, which suggest that the adsorption following the Sips isotherm model is an amalgamation of the Langmuir (chemisorption) and Freundlich (physisorption) isotherm model.

Effect of different water samples
The adsorption of VB was evaluated in four varied types of water matrices, as illustrated in Fig. 12. Mineral, tap, and lake water were the three kinds of water models collected, and they were equated with distilled water[92]. 50 mL of 100 ppm dye solution was made using the water samples, and 12 mg of nanocomposite was mixed and agitated for about 1 h. Out of the three, mineral water was the purest, showing a removal efficiency of 47.62%, whereas, in the case of tap water and lake water, the efficiency slumped up to 39.818% and 31.13%, respectively. Due to the presence of different inhibitory inorganic ions and organic substances in the previously mentioned
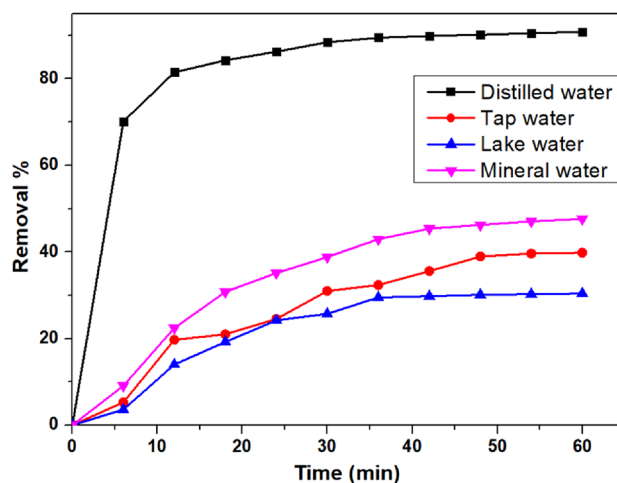
Figure 12. Effect of different water samples on the removal of VB.

water matrices at varied concentrations, the removal capacity of the adsorbent is usually decreased in these environmental waters. Because lake water contains more extra pollutants and surfactants than tap water, it may have been less effective as an adsorbent in the previous matrix.

Effect of organic compounds

Studies explored the influence of organic compounds such as acetone, butanol, and sodium dodecyl sulfate (SDS) on the adsorption of VB dye by CS/In_2S_3 nanocomposite. Acetone is widely used in industry and everyday life because of its excellent solvent properties[93]. Butanol is used as a solvent for chemical reactions and is considered a potential gasoline replacement, whereas SDS is a surfactant and is commonly present in house cleansing products[94]. As illustrated in Fig. 13, 12 mg of nanocomposite was added to 100 ppm of VB dye, and the adsorption efficiency was investigated under different concentrations of organic compounds. Acetone and butanol, two commonly used solvents, exhibit a relatively strong quenching effect and have regeneration capabilities[95]. 1 M of acetone and butanol decreased the removal efficiency to 56.02% and 59.36%, respectively. The molecules of acetone and butanol competed with dye molecules for active surfaces as their increased concentration resulted in decreased dye adsorption. The dye sorption increased as the SDS surfactant concentration increased slightly (10 ppm)[96]. However, as the surfactant concentration increased further, the dye sorption was significantly suppressed by micelle formation and dye solubilization and was reduced to 58.61% at 40 ppm of SDS concentration.

Effect of inorganic salts

The impact on the adsorption of dyes by inorganic salts has been examined in many research[97,98]. In this work, 0.01 M of salts such as $NaCl$, $CaCl_2$, $AlCl_3$, Na_2SO_4, and CH_3COONa were introduced to 50 mL of 100 ppm VB dye to which 12 mg of nanocomposite was added to study the effect of cations (Fig. 14a) and anions (Fig. 14b). The addition of inorganic salts results in a reduction in adsorption efficacy as they might reduce the surface charge of the fabricated CS/In_2S_3 nanocomposite[99]. Due to the competition between ions formed by the hydrolysis of salts and organic molecules for adsorption sites, adsorption efficiency is slightly reduced[100]. In addition, these ions contest with VB molecules at adsorption sites, reducing VB's electrostatic attraction onto CS/In_2S_3 nanocomposite[101]. Due to inorganic cations, the removal efficiency slumped to 67.73, 63.72, and 55.14% for Na^+, Ca^{2+}, and Al^{3+}, respectively, whereas for inorganic anions, the removal percentage decreased to 67.73, 36.81, and 10.95% for Cl^-, SO_4^{2-}, and CH_3COO^-, respectively.

Adsorption mechanism

The higher adsorption capacity of the CS/In_2S_3 nanocomposite for adsorbing VB can be credited to the -OH functional groups of chitosan (Fig. 15a), as its small surface area, high porosity, and high crystalline property increases its efficiency[102]. The functional groups in chitosan were assessed using FTIR spectroscopy to study the mechanism. The FTIR spectrum of CS/In_2S_3 nanocomposite is demonstrated in Fig. 15b. A high-intensity band at 3343–3232 cm^{-1} specifies N–H and O–H stretchings aroused due to hydrogen bonding in chitosan, overlying in the equivalent region. The 2931 cm^{-1} to 2861 cm^{-1} peaks designate symmetric and asymmetric stretching of C-H bonds. These bands are polysaccharide-specific and may be detected in the spectra of other polysaccharides such as xylan[103], glucans[104], and carrageenans[105]. The bands around 1635 cm^{-1} and 1590 cm^{-1} could be accredited to amide groups. Absorption bands at 1371 cm^{-1} and 617 cm^{-1} specify the vibration modes of the In-S band in In_2S_3[106]. A new strong peak appeared at 1575 cm^{-1} in the FTIR spectrum of CS/In_2S_3 after 5 cycles and can be allocated to N–H bending of a primary amine in chitosan overlapping with N–H group of adsorbed VB dye on chitosan surface[107]. A small peak around 880 cm^{-1} could be due to the plane bending of C-H in the polysaccharide ring. The increased intensity of the band at 1371 cm^{-1}, which is the distinguishing
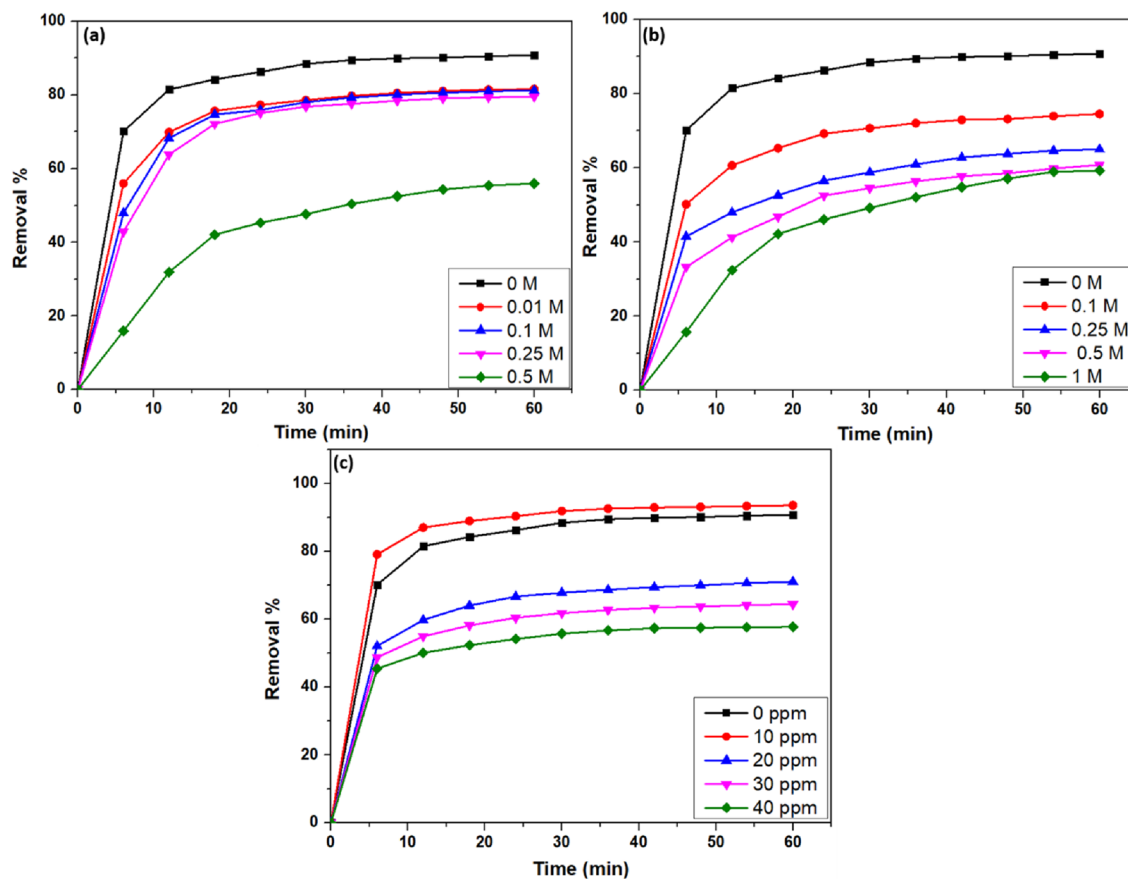
Figure 13. Impact of (**a**) acetone, (**b**) butanol, and (**c**) SDS on the removal of VB.

stretching of the CH_3 stretching, could be due to the improved number of CH_3 groups from the adsorbed VB molecules[108]. An absorption band could confirm the asymmetric stretching of the C–O–C group at 1152 cm^{-1}. The bands situated at 1062 cm^{-1} and 1020 cm^{-1} correspond to the stretching of C-O bonds. All of these bands correlate well with the FTIR spectra of chitosan that were previously published[109,110]. The peaks around 3360 cm^{-1} (N–H),1640 cm^{-1} (amide I), 1148 cm^{-1} (C–N), and 1020 cm^{-1} (C–O) imply that the adsorption of dye was onto the hydroxyl groups of chitosan via covalent bonding[111].

Reusability analysis

As it is imperative to assess the efficacy of the adsorbent from a re-application standpoint and from an economic perspective, the reusability of the adsorbent is analyzed (Fig. 16a). The dye was regenerated using acetone as a desorption media. 20 mL of acetone was added to the filtered nanocomposite, and then it was thoroughly shaken for 30 min, and the supernatant was centrifuged. Further, the derived nanocomposite was cleaned with de-ionized water and desiccated for further adsorption analysis for five cycles. The 2nd run showed an efficiency of 90.35%, while the removal efficiency slumped to 75.07% during the 5th cycle, as shown in Fig. 16b. This reduction in the removal ability in the 5th cycle may be due to the disintegration of the active sites. Moreover, no significant change in the FTIR bands, as shown in Fig. 15b, indicates the high stability and reusability of the prepared adsorbent after five cycles. In addition, the XRD plot (Fig. 16c) and TEM image (Fig. 16d) of the nanocomposite after five cycles confirm the constancy of the fabricated nanocomposite.
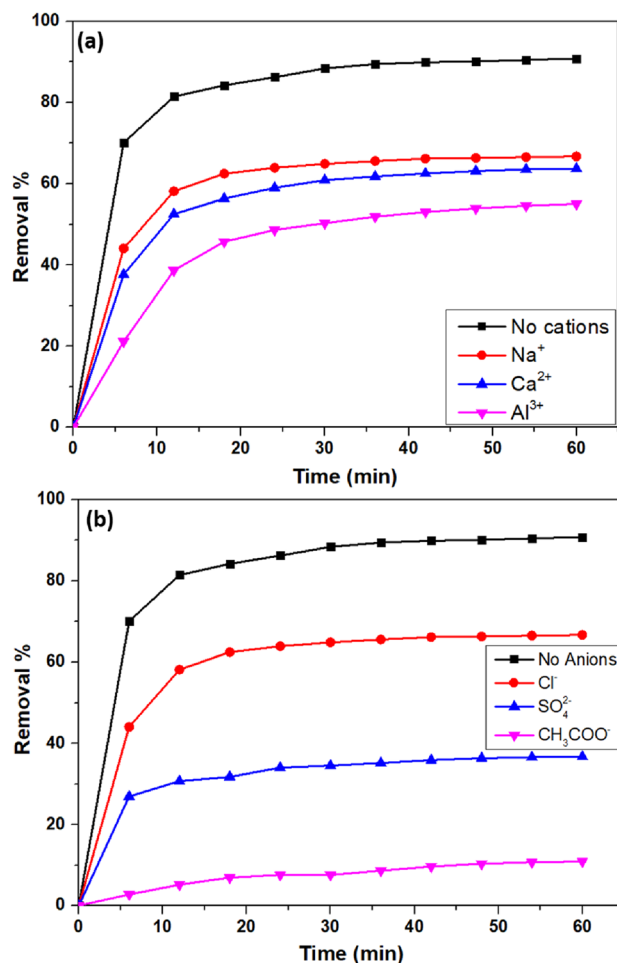
Figure 14. Role of (**a**) inorganic cations and (**b**) inorganic anions on the removal of VB.

Conclusion

CS/In_2S_3 nanocomposite was manufactured by a facile co-precipitation method. The adsorption studies were conducted to understand the various aspects influencing the removal performance, for example, the initial concentration of the dye, adsorbent dosage, and contact time. The effect of temperature and thermodynamic studies is also carried out, along with the impact of various organic compounds, inorganic salts, and water matrices on VB adsorption. The nanocomposite was characterized to assign its structure, texture, morphology, and chemical composition. XRD, TEM-SAED, SEM, EDAX, XPS, Elemental Mapping, FTIR, and BET analyses were conducted to characterize the nanocomposite. The HR-TEM images show the accumulation of the In_2S_3 nanoparticles on the CS polymer matrix. The nanocomposite showed an appreciable q_m of 683.34 mg g^{-1} and an excellent removal efficiency of 90.81% for the 100 ppm VB dye removal using 12 mg (0.24 g L^{-1}) of the nanocomposite. The BET isotherm of the nanohybrid showed type I hysteresis and type IV adsorption curves. Also, the adsorption performance is defined by the Sips adsorption isotherm and PSO kinetics having the value of rate constant k_2 of 6.357×10^{-3} g mg^{-1} min^{-1}. The sips adsorption isotherm model was a combination of Langmuir and Freundlich's adsorption isotherm model, and the adsorption mechanism was further investigated using SPM. The SPM interpreted the bonded number of dye molecules, the density of adsorption sites, the saturation adsorption capacity of adsorbent, and adsorption energies, which helped in understanding the mechanism of adsorption of VB on fabricated novel CS/In_2S_3 nanocomposite. From this, it can be inferred that the nanocomposite adsorbed the dye molecules in a mixed orientation involving multi-molecular and multi-interaction mechanisms. Moreover, the nanocomposite showed excellent stability and was reusable up to 5 times.
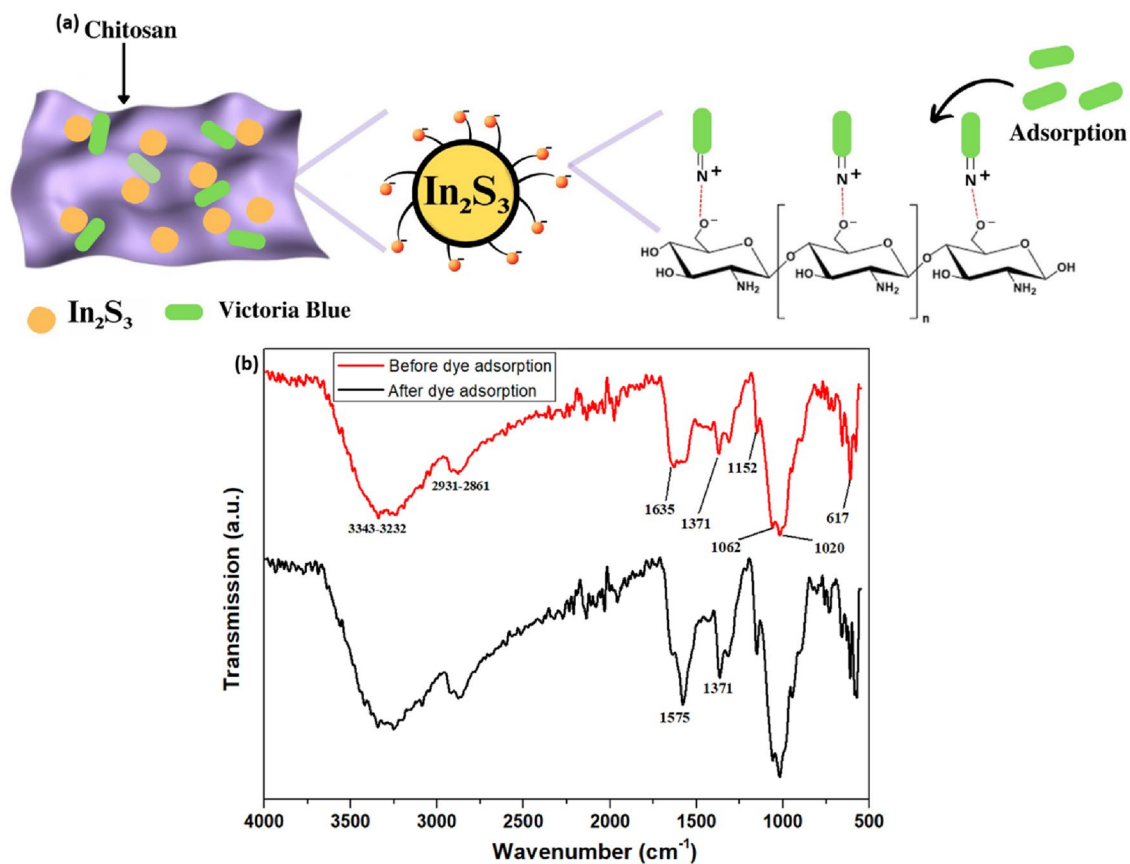
Figure 15. (**a**) Plausible mechanism of dye adsorption by fabricated CS/In$_2$S$_3$ adsorbent; (**b**) FTIR spectrum before and after adsorption.
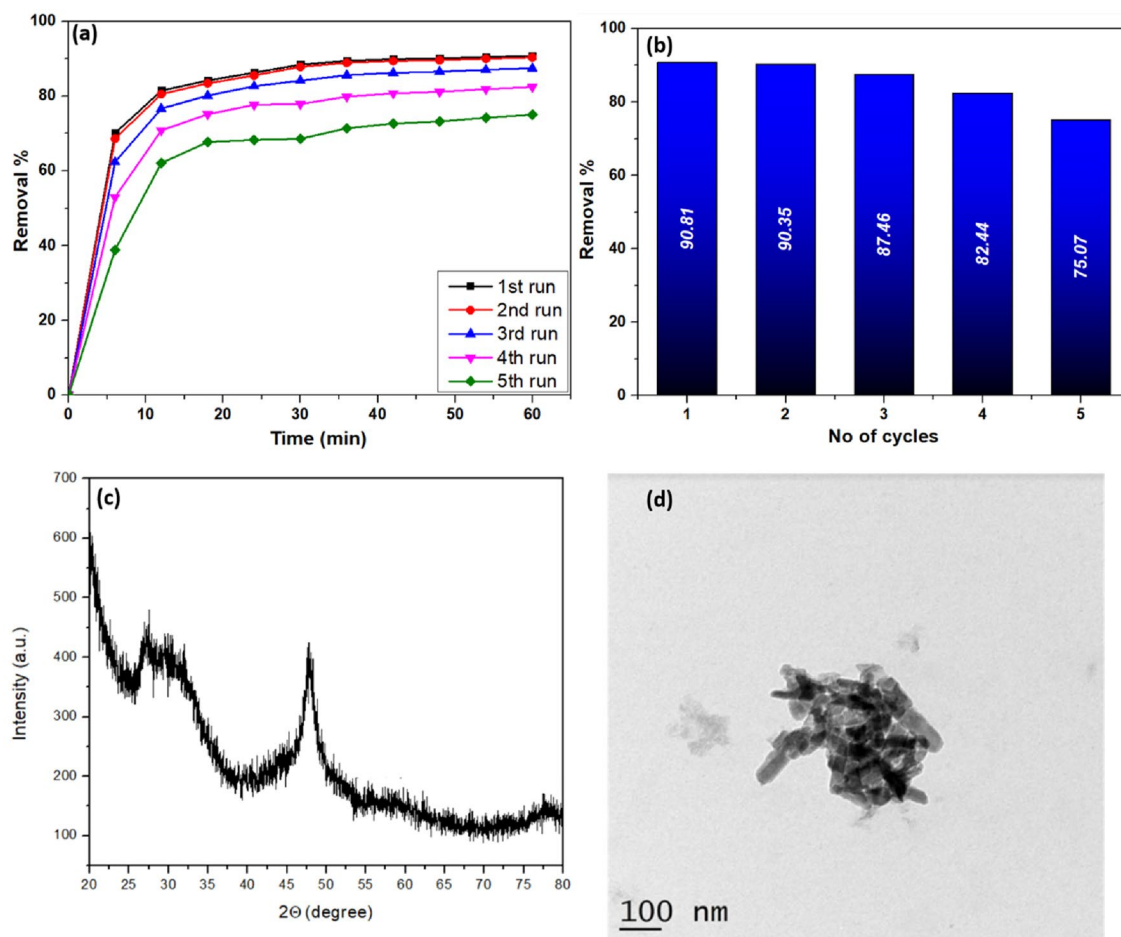
Figure 16. (**a**) Efficiency of VB removal, (**b**) Graph showing removal percentage during various cycles, (**c**) XRD plot, and (**d**) TEM image after dye adsorption.

Data availability

All data generated or analyzed during this study are included in this published article.

References

1. Mishra, S. R., Gadore, V. & Ahmaruzzaman, M. Development of high-performance bi-functional novel CdSnS 2 atom clusters for adsorption of rose Bengal and AOP-assisted degradation of methylene blue. *Environ. Sci. Water Res. Technol.* **9**, 586–602. https://doi.org/10.1039/D2EW00654E (2023).
2. Mishra, S. R. *et al.* In2S3 incorporated into CO32−@Ni/Fe/Zn trimetallic LDH as a bi-functional novel nanomaterial for enzymatic urea sensing and removal of sulfur-containing pharmaceutical from aqueous streams. *Chem. Eng. J.* https://doi.org/10.1016/J.CEJ.2023.146207 (2023).
3. Asfaram, A., Ghaedi, M., Agarwal, S., Tyagi, I. & Gupta, V. K. Removal of basic dye Auramine-O by ZnS: Cu nanoparticles loaded on activated carbon: optimization of parameters using response surface methodology with central composite design. *RSC Adv.* **5**, 18438–18450. https://doi.org/10.1039/C4RA15637D (2015).
4. Mishra, S. R., Gadore, V. & Ahmaruzzaman, M. A critical review on In2S3-based nanomaterial for emerging contaminants elimination through integrated adsorption-degradation technique: Effect of reaction parameters and co-existing species. *J. Hazard. Mater. Lett.* **4**, 100087. https://doi.org/10.1016/J.HAZL.2023.100087 (2023).
5. Mishra, S. R. & Ahmaruzzaman, M. CuO and CuO-based nanocomposites: Synthesis and applications in environment and energy. *Sustain. Mater. Technol.* **33**, e00463. https://doi.org/10.1016/J.SUSMAT.2022.E00463 (2022).
6. Yadav, G., Yadav, N., Sultana, M. & Ahmaruzzaman, M. A comprehensive review on low-cost waste-derived catalysts for environmental remediation. *Mater. Res. Bull.* **164**, 112261. https://doi.org/10.1016/J.MATERRESBULL.2023.112261 (2023).
7. Bhattacharjee, B., Ahmaruzzaman, M., Djellabi, R., Elimian, E. & Rtimi, S. Advances in 2D MXenes-based materials for water purification and disinfection: Synthesis approaches and photocatalytic mechanistic pathways. *J. Environ. Manage.* **324**, 116387. https://doi.org/10.1016/J.JENVMAN.2022.116387 (2022).
8. Morgan, J., Whitaker, J. E. & Oseroff, A. R. GRP78 induction by calcium Ionophore potentiates photodynamic therapy using the mitochondrial targeting dye victoria blue BO. *Photochem. Photobiol.* **67**, 155–164. https://doi.org/10.1111/J.1751-1097.1998.TB05179.X (1998).
9. Khan, T. A., Nouman, M., Dua, D., Khan, S. A. & Alharthi, S. S. Adsorptive scavenging of cationic dyes from aquatic phase by H₃PO₄ activated Indian jujube (Ziziphus mauritiana) seeds based activated carbon: Isotherm, kinetics, and thermodynamic study. *J. Saudi Chem. Soc.* **26**, 101417. https://doi.org/10.1016/J.JSCS.2021.101417 (2022).

10. Zhou, M. *et al.* The coupling of persulfate activation and membrane separation for the effective pollutant degradation and membrane fouling alleviation. *Chem. Eng. J.* **451**, 139009 (2023).

11. Gadore, V., Mishra, S. R. & Ahmaruzzaman, M. Bio-inspired sustainable synthesis of novel SnS$_2$/biochar nanocomposite for adsorption coupled photodegradation of amoxicillin and congo red: Effects of reaction parameters, and water matrices. *J. Environ. Manage.* **334**, 117496. https://doi.org/10.1016/J.JENVMAN.2023.117496 (2023).

12. Gadore, V., Ranjan Mishra, S. & Ahmaruzzaman, M. SnS$_2$ modified carbonate-intercalated Ni-Zn-Fe trimetallic LDH as a novel photocatalyst for persulfate activation: Influence of operational parameters, co-existing ions and organic compounds. *Chem. Eng. J.* **475**, 146157 (2023).

13. Yadav, G., Mishra, S. R., Gadore, V., Yadav, N. & Ahmaruzzaman, M. A smart and sustainable pathway for abatement of single and binary mixtures of dyes through magnetically retrievable Ca$_4$Fe$_9$O$_{17}$ anchored on Biochar matrix. *Sci. Rep.* **131**(13), 1–21. https://doi.org/10.1038/s41598-023-40077-w (2023).

14. Babar, M. *et al.* Comparative study of ozonation and ozonation catalyzed by Fe-loaded biochar as catalyst to remove methylene blue from aqueous solution. *Chemosphere.* **307**, 135738. https://doi.org/10.1016/J.CHEMOSPHERE.2022.135738 (2022).

15. Liu, Y., Wang, J. Multivalent metal catalysts in Fenton/Fenton-like oxidation system: A critical review, Chem. Eng. J. 143147 (2023).

16. Yadav, G. & Ahmaruzzaman, M. Recent development of novel nanocomposites for photocatalysis mediated remediation of phenolic derivatives: A comprehensive review. *J. Ind. Eng. Chem.* **127**, 18–35. https://doi.org/10.1016/J.JIEC.2023.07.029 (2023).

17. Mishra, S. R., Gadore, V., Ghotekar, S. & Ahmaruzzaman, M. Insights into the enhanced photocatalytic and antioxidant properties of novel biogenically synthesised β-In2S3 quantum dots. *Int. J. Environ. Anal. Chem.* https://doi.org/10.1080/03067319.2023.2186228 (2023).

18. Mishra, S. R., Gadore, V. & Ahmaruzzaman, M. Recent advances in In$_2$S$_3$-based photocatalysts for catalytic reduction of CO$_2$. *Chem. Phys. Impact.* **7**, 100324. https://doi.org/10.1016/J.CHPHI.2023.100324 (2023).

19. Belal, R. M., Zayed, M. A., El-Sherif, R. M. & Ghany, N. A. A. Electrochemical degradation and degree of mineralization of the BY28 dye in a supporting electrolyte mixture using an expanded dimensionally stable anode. *Electrocatalysis.* **13**, 26–36. https://doi.org/10.1007/S12678-021-00680-9/TABLES/2 (2022).

20. Kurade, M. B. *et al.* Integrated phycoremediation and ultrasonic-irradiation treatment (iPUT) for the enhanced removal of pharmaceutical contaminants in wastewater. *Chem. Eng. J.* **455**, 140884 (2023).

21. Chen, B. *et al.* Global distribution of marine microplastics and potential for biodegradation. *J. Hazard. Mater.* **451**, 131198 (2023).

22. Bhuyan, A. & Ahmaruzzaman, M. Metal-organic frameworks: A new generation potential material for aqueous environmental remediation. *Inorg. Chem. Commun.* **140**, 109436. https://doi.org/10.1016/J.INOCHE.2022.109436 (2022).

23. Grich, A. *et al.* Preparation of low-cost activated carbon from Doum fiber (Chamaerops humilis) for the removal of methylene blue: Optimization process by DOE/FFD design, characterization, and mechanism. *J. Mol. Struct.* **1295**, 136534. https://doi.org/10.1016/J.MOLSTRUC.2023.136534 (2024).

24. Gadore, V., Mishra, S. R. & Ahmaruzzaman, M. Metal sulphides and their heterojunctions for photocatalytic degradation of organic dyes-A comprehensive review. *Environ. Sci. Pollut. Res.* **2023**(1), 1–48. https://doi.org/10.1007/S11356-023-28753-W (2023).

25. Crini, G. & Badot, P. M. Application of chitosan, a natural aminopolysaccharide, for dye removal from aqueous solutions by adsorption processes using batch studies: A review of recent literature. *Prog. Polym. Sci.* **33**, 399–447. https://doi.org/10.1016/J.PROGPOLYMSCI.2007.11.001 (2008).

26. Yaashikaa, P. R., Senthil Kumar, P. & Karishma, S. Review on biopolymers and composites—Evolving material as adsorbents in removal of environmental pollutants. *Environ. Res.* **212**, 113114. https://doi.org/10.1016/J.ENVRES.2022.113114 (2022).

27. Rangraz, Y., Nemati, F. & Elhampour, A. Magnetic chitosan composite as a green support for anchoring diphenyl diselenide as a biocatalyst for the oxidation of sulfides. *Int. J. Biol. Macromol.* **117**, 820–830. https://doi.org/10.1016/J.IJBIOMAC.2018.05.207 (2018).

28. Naghipour, A. & Fakhri, A. Heterogeneous Fe3O4@chitosan-Schiff base Pd nanocatalyst: Fabrication, characterization and application as highly efficient and magnetically-recoverable catalyst for Suzuki-Miyaura and Heck-Mizoroki C-C coupling reactions. *Catal. Commun.* **73**, 39–45. https://doi.org/10.1016/J.CATCOM.2015.10.002 (2016).

29. Muzzarelli, R. A. A. *et al.* Current views on fungal chitin/chitosan, human chitinases, food preservation, glucans, pectins and inulin: A tribute to Henri Braconnot, precursor of the carbohydrate polymers science, on the chitin bicentennial. *Carbohydr. Polym.* **87**, 995–1012. https://doi.org/10.1016/J.CARBPOL.2011.09.063 (2012).

30. Oukhrib, R. *et al.* DFT, Monte Carlo and molecular dynamics simulations for the prediction of corrosion inhibition efficiency of novel pyrazolylnucleosides on Cu(111) surface in acidic media. *Sci. Reports* **111**(11), 1–18. https://doi.org/10.1038/s41598-021-82927-5 (2021).

31. Oladzadabbasabadi, N. *et al.* Recent advances in extraction, modification, and application of chitosan in packaging industry. *Carbohydr. Polym.* **277**, 118876. https://doi.org/10.1016/J.CARBPOL.2021.118876 (2022).

32. Souissi, R., Bouguila, N. & Labidi, A. Ethanol sensing properties of sprayed β-In2S3 thin films. *Sensors Actuators B Chem.* **261**, 522–530. https://doi.org/10.1016/J.SNB.2018.01.175 (2018).

33. George, J., Joseph, K. S., Pradeep, B. & Palson, T. I. Reactively evaporated films of indium sulphide. *Phys. Status Solidi.* **106**, 123–131. https://doi.org/10.1002/PSSA.2211060116 (1988).

34. Raouf Hosseini, M. & Nasiri Sarvi, M. Recent achievements in the microbial synthesis of semiconductor metal sulfide nanoparticles. *Mater. Sci. Semicond. Process.* **40**, 293–301. https://doi.org/10.1016/J.MSSP.2015.06.003 (2015).

35. Zhou, M. *et al.* Spherical In$_2$S$_3$ anchored on g-C$_3$N$_4$ nanosheets for efficient elemental mercury removal in the wide temperature range. *Chem. Eng. J.* **430**, 132857. https://doi.org/10.1016/J.CEJ.2021.132857 (2022).

36. Cheng, Y. *et al.* Highly stable hierarchical flower-like β-In2S3 assembled from 2D nanosheets with high adsorption-photodecolorization activities for the treatment of wastewater. *J. Nanoparticle Res.* **19**, 1–15. https://doi.org/10.1007/S11051-017-3858-Y/FIGURES/10 (2017).

37. Ranjan Mishra, S., Gadore, V. & Ahmaruzzaman, M. Novel 3D sphere-like β-In2S3/Biochar nanoflowers for remediation of dyes in single and binary systems and interpretation using statistical physical modeling. *Environ. Nanotechnol. Monit. Manag.* **20**, 100807. https://doi.org/10.1016/J.ENMM.2023.100807 (2023).

38. Li, Z. *et al.* Interpretation of the adsorption mechanism of Reactive Black 5 and Ponceau 4R dyes on chitosan/polyamide nanofibers via advanced statistical physics model. *J. Mol. Liq.* **285**, 165–170. https://doi.org/10.1016/J.MOLLIQ.2019.04.091 (2019).

39. Kennedy, A. *et al.* An effect of metal ions (Cu, Mn) doping on the structural, morphological, optical, photoluminescence electrical and photocatalytic properties of In2S3 nanoparticles. *Opt. Mater. Amst.* **124**, 111769. https://doi.org/10.1016/J.OPTMAT.2021.111769 (2022).

40. Gadore, V., Mishra, S. R. & Ahmaruzzaman, M. Green and environmentally sustainable fabrication of SnS2 quantum dots/chitosan nanocomposite for enhanced photocatalytic performance: Effect of process variables, and water matrices. *J. Hazard. Mater.* **444**, 130301. https://doi.org/10.1016/J.JHAZMAT.2022.130301 (2023).

41. Kausar, A. Polymer and modified chitosan-based nanocomposite: impending material for technical application. *Polym.-Plastics Technol. Mater.* **58**(9), 934–947. https://doi.org/10.1080/25740881.2019.1587771 (2019).

42. Aziz, S. B., Abdulwahid, R. T., Rasheed, M. A., Abdullah, O. G. H. & Ahmed, H. M. Polymer blending as a novel approach for tuning the SPR peaks of silver nanoparticles. *Polym.* **2017**(9), 486. https://doi.org/10.3390/POLYM9100486 (2017).

43. Rengaraj, S. *et al.* Self-assembled mesoporous hierarchical-like In2S3 hollow microspheres composed of nanofibers and nanosheets and their photocatalytic activity. *Langmuir.* **27**, 5534–5541 (2011).

44. Revathi, N., Prathap, P., Subbaiah, Y. P. V. & Reddy, K. T. R. Substrate temperature dependent physical properties of In2S3 films. *J. Phys. D. Appl. Phys.* **41**, 155404. https://doi.org/10.1088/0022-3727/41/15/155404 (2008).

45. Pathania, D. *et al.* Photocatalytic degradation of highly toxic dyes using chitosan-g-poly(acrylamide)/ZnS in presence of solar irradiation. *J. Photochem. Photobiol. A Chem.* **329**, 61–68. https://doi.org/10.1016/J.JPHOTOCHEM.2016.06.019 (2016).

46. Sirajudheen, P., Resha Kasim, V. C., Nabeena, C. P., Basheer, M. C. & Meenakshi, S. Tunable photocatalytic oxidation response of ZnS tethered chitosan-polyaniline composite for the removal of organic pollutants: A mechanistic perspective. *Mater. Today Proc.* **47**, 2553–2559. https://doi.org/10.1016/J.MATPR.2021.05.054 (2021).

47. Raha, S. & Ahmaruzzaman, M. Enhanced performance of a novel superparamagnetic g-C3N4/NiO/ZnO/Fe3O4 nanohybrid photocatalyst for removal of esomeprazole: Effects of reaction parameters, co-existing substances and water matrices. *Chem. Eng. J.* **395**, 124969. https://doi.org/10.1016/j.cej.2020.124969 (2020).

48. Mishra, S. R., Gadore, V. & Ahmaruzzaman, M. Insights into persulfate-activated photodegradation of tinidazole and photoreduction of hexavalent chromium through β-In2S3 anchored on Ag-doped fish scale-derived HAp composite quantum dots. *J. Clean. Prod.* **427**, 139221. https://doi.org/10.1016/J.JCLEPRO.2023.139221 (2023).

49. Deminskyi, P., Rouf, P., Ivanov, I. G. & Pedersen, H. Atomic layer deposition of InN using trimethylindium and ammonia plasma. *J. Vac. Sci. Technol. A Vacuum Surf. Film.* **37**, 020926 (2019).

50. Gunavathy, K. V. *et al.* Highly improved photo-sensing ability of In$_2$S$_3$ thin films through cerium doping. *Opt. Mater. Amst.* **137**, 113612. https://doi.org/10.1016/J.OPTMAT.2023.113612 (2023).

51. Daniyal, W. M. E. M. M. *et al.* X-ray photoelectron spectroscopy analysis of chitosan-graphene oxide-based composite thin films for potential optical sensing applications. *Polym.* **13**, 478 (2021).

52. Gieroba, B. *et al.* Spectroscopic studies on the temperature-dependent molecular arrangements in hybrid chitosan/1,3-β-D-glucan polymeric matrices. *Int. J. Biol. Macromol.* **159**, 911–921. https://doi.org/10.1016/J.IJBIOMAC.2020.05.155 (2020).

53. Yadav, N., Yadav, G. & Ahmaruzzaman, M. Fabrication of surface-modified dual waste-derived biochar for biodiesel production by microwave-assisted esterification of oleic acid: Optimization, kinetics, and mechanistic studies. *Renew. Energy.* **218**, 119308. https://doi.org/10.1016/J.RENENE.2023.119308 (2023).

54. Rouquerol, J., Rouquerol, F., Llewellyn, P., Maurin, G., Sing, K. Adsorption by powders and porous solids: principles, methodology and applications, Academic press, (2013).

55. Cychosz, K. A. & Thommes, M. Progress in the physisorption characterization of nanoporous gas storage materials. *Engineering.* **4**, 559–566. https://doi.org/10.1016/J.ENG.2018.06.001 (2018).

56. Salem, A. N. M., Ahmed, M. A. & El-Shahat, M. F. Selective adsorption of amaranth dye on Fe$_3$O$_4$/MgO nanoparticles. *J. Mol. Liq.* **219**, 780–788. https://doi.org/10.1016/J.MOLLIQ.2016.03.084 (2016).

57. Gopal, V. L. & Chellapandian, K. Synthesis of hybrid framework of tenorite and octahedrally coordinated aluminosilicate for the robust adsorption of cationic and anionic dyes. *Environ. Res.* **220**, 115111. https://doi.org/10.1016/J.ENVRES.2022.115111 (2023).

58. Chaudhary, S., Goyal, S. & Umar, A. Fabrication of biogenic carbon-based materials from coconut husk for the eradication of dye. *Chemosphere.* **340**, 139823. https://doi.org/10.1016/J.CHEMOSPHERE.2023.139823 (2023).

59. Guerra, D. L., Batista, A. C. & P.C. Corrêa da costa, R.R. Viana, C. Airoldi,. Adsorption of arsenic ions on Brazilian sepiolite: Effect of contact time, pH, concentration, and calorimetric investigation. *J. Colloid Interface Sci.* **346**, 178–187. https://doi.org/10.1016/J.JCIS.2010.02.041 (2010).

60. Liu, X. *et al.* Enhanced dyes adsorption from wastewater via Fe3O4 nanoparticles functionalized activated carbon. *J. Hazard. Mater.* **373**, 397–407. https://doi.org/10.1016/J.JHAZMAT.2019.03.103 (2019).

61. Afkhami, A. & Moosavi, R. Adsorptive removal of Congo red, a carcinogenic textile dye, from aqueous solutions by maghemite nanoparticles. *J. Hazard. Mater.* **174**, 398–403. https://doi.org/10.1016/J.JHAZMAT.2009.09.066 (2010).

62. Langmuir, I. The adsorption of gases on plane surfaces of glass, mica and platinum. *J. Am. Chem. Soc.* **40**, 1361–1403. https://doi.org/10.1021/JA02242A004/ASSET/JA02242A004.FP.PNG_V03 (1918).

63. Freundlich, H. & Heller, W. The Adsorption of cis- and trans-Azobenzene. *J. Am. Chem. Soc.* **61**, 2228–2230. https://doi.org/10.1021/JA01877A071/ASSET/JA01877A071.FP.PNG_V03 (1939).

64. Sips, R. On the Structure of a Catalyst Surface. *J. Chem. Phys.* **16**, 490. https://doi.org/10.1063/1.1746922 (2004).

65. Redlich, O. & Peterson, D. L. A useful adsorption isotherm. *J. Phys. Chem.* **63**, 1024. https://doi.org/10.1021/J150576A611/ASSET/J150576A611.FP.PNG_V03 (1959).

66. Revellame, E. D., Fortela, D. L., Sharp, W., Hernandez, R. & Zappi, M. E. Adsorption kinetic modeling using pseudo-first order and pseudo-second order rate laws: A review. *Clean. Eng. Technol.* **1**, 100032. https://doi.org/10.1016/J.CLET.2020.100032 (2020).

67. Ezzati, R. Derivation of pseudo-first-order, pseudo-second-order and modified pseudo-first-order rate equations from Langmuir and Freundlich isotherms for adsorption. *Chem. Eng. J.* **392**, 123705 (2020).

68. Aharoni, C., Tompkins, F.C. Kinetics of adsorption and desorption and the Elovich equation, in: Adv. Catal., Elsevier, 1970: pp. 1–49.

69. Abbasi, A. & Ikram, S. Fabrication of a novel green bio-composite for sequestration of Victoria Blue from aquatic medium: Isotherm, Kinetics, and Thermodynamic investigations. *Chem. Phys. Lett.* **800**, 139665. https://doi.org/10.1016/J.CPLETT.2022.139665 (2022).

70. Mirzajani, R., Pourreza, N., Zayadi, A., Malakooti, R. & Mahmoodi, H. Nanoporous calcined MCM-41 silica for adsorption and removal of Victoria blue dye from different natural water samples. *New Pub Balaban.* **57**, 5903–5913. https://doi.org/10.1080/19443994.2015.1005690 (2015).

71. Jain, S. N. *et al.* Incense stick ash as a novel and sustainable adsorbent for sequestration of Victoria Blue from aqueous phase. *Sustain. Chem. Pharm.* **15**, 100199. https://doi.org/10.1016/J.SCP.2019.100199 (2020).

72. Kataria, N., Garg, V. K., Jain, M. & Kadirvelu, K. Preparation, characterization and potential use of flower shaped Zinc oxide nanoparticles (ZON) for the adsorption of Victoria Blue B dye from aqueous solution. *Adv. Powder Technol.* **27**, 1180–1188. https://doi.org/10.1016/J.APT.2016.04.001 (2016).

73. Kumar, M., Tamilarasan, R. & Sivakumar, V. Adsorption of Victoria blue by carbon/Ba/alginate beads: Kinetics, thermodynamics and isotherm studies. *Carbohydr. Polym.* **98**, 505–513. https://doi.org/10.1016/J.CARBPOL.2013.05.078 (2013).

74. Gupta, S.V., Ahmaruzzaman, M. Development of efficient magnetic Fe$_2$O$_3$-activated Bakelite nanocomposite as an adsorbent for removal of Victoria blue dye from water (2021) http://doi.org/10.1080/03067319.2020.1843025.

75. Banerjee, S., Sharma, G. C., Dubey, S. & Sharma, Y. C. Adsorption characteristics of a low cost activated carbon for the removal of victoria blue from aqueous solutions. *J. Mater. Environ. Sci.* **6**, 2045–2052 (2015).

76. Salman, M., Athar, M. & Farooq, U. Biosorption of heavy metals from aqueous solutions using indigenous and modified lignocellulosic materials. *Rev. Environ. Sci. Biotechnol.* **14**, 211–228. https://doi.org/10.1007/S11157-015-9362-X/TABLES/6 (2015).

77. Milonjić, S. K. A consideration of the correct calculation of thermodynamic parameters of adsorption. *J. Serbian Chem. Soc.* **72**, 1363–1367. https://doi.org/10.2298/JSC0712363M (2007).

78. Singh, T. S. & Pant, K. K. Equilibrium, kinetics and thermodynamic studies for adsorption of As(III) on activated alumina. *Sep. Purif. Technol.* **36**, 139–147. https://doi.org/10.1016/S1383-5866(03)00209-0 (2004).

79. Thamer, B. M., Al-aizari, F. A. & Hameed, M. M. A. Zero-valent Ni/NiO core-shell nanosheets supported on graphene for highly efficient dye adsorption: Isotherm, kinetic and thermodynamic study. *Chem. Eng. Res. Des.* **197**, 656–668. https://doi.org/10.1016/J.CHERD.2023.08.023 (2023).

80. Li, M. *et al.* Different mechanisms for E. coli disinfection and BPA degradation by CeO_2-AgI under visible light irradiation. *Chem. Eng. J.* **371**, 750–758. https://doi.org/10.1016/J.CEJ.2019.04.036 (2019).

81. Sellaoui, L., Dotto, G. L., Ben Lamine, A. & Erto, A. Interpretation of single and competitive adsorption of cadmium and zinc on activated carbon using monolayer and exclusive extended monolayer models. *Environ. Sci. Pollut. Res.* **24**, 19902–19908. https://doi.org/10.1007/S11356-017-9562-8/TABLES/1 (2017).

82. Li, Z., Sellaoui, L., Luiz Dotto, G., Bonilla-Petriciolet, A. & Ben Lamine, A. Understanding the adsorption mechanism of phenol and 2-nitrophenol on a biopolymer-based biochar in single and binary systems via advanced modeling analysis. *Chem. Eng. J.* **371**, 1–6. https://doi.org/10.1016/J.CEJ.2019.04.035 (2019).

83. You, X., Zhou, R., Zhu, Y., Bu, D. & Cheng, D. Adsorption of dyes methyl violet and malachite green from aqueous solution on multi-step modified rice husk powder in single and binary systems: Characterization, adsorption behavior and physical interpretations. *J. Hazard. Mater.* **430**, 128445. https://doi.org/10.1016/J.JHAZMAT.2022.128445 (2022).

84. Selim, A. Q. *et al.* Statistical physics-based analysis of the adsorption of Cu2+ and Zn2+ onto synthetic cancrinite in single-compound and binary systems. *J. Environ. Chem. Eng.* **7**, 103217. https://doi.org/10.1016/J.JECE.2019.103217 (2019).

85. Azha, S. F. *et al.* Synthesis and characterization of a novel amphoteric adsorbent coating for anionic and cationic dyes adsorption: Experimental investigation and statistical physics modelling. *Chem. Eng. J.* **351**, 221–229. https://doi.org/10.1016/J.CEJ.2018.06.092 (2018).

86. Dhaouadi, F. *et al.* Adsorption of methylene blue on comminuted raw avocado seeds: Interpretation of the effect of salts via physical monolayer model. *J. Mol. Liq.* **305**, 112815. https://doi.org/10.1016/J.MOLLIQ.2020.112815 (2020).

87. Wang, H. *et al.* Effective adsorption of dyes on an activated carbon prepared from carboxymethyl cellulose: Experiments, characterization and advanced modelling. *Chem. Eng. J.* **417**, 128116. https://doi.org/10.1016/J.CEJ.2020.128116 (2021).

88. Li, Z. *et al.* Adsorption of congo red and methylene blue dyes on an ashitaba waste and a walnut shell-based activated carbon from aqueous solutions: Experiments, characterization and physical interpretations. *Chem. Eng. J.* **388**, 124263. https://doi.org/10.1016/J.CEJ.2020.124263 (2020).

89. Sellaoui, L. *et al.* Application of a multilayer physical model for the critical analysis of the adsorption of nicotinamide and propranolol on magnetic-activated carbon. *Environ. Sci. Pollut. Res.* **29**, 30184–30192. https://doi.org/10.1007/S11356-021-18483-2/FIGURES/6 (2022).

90. Wang, X. *et al.* Adsorption of azo dyes and Naproxen by few-layer MXene immobilized with dialdehyde starch nanoparticles: Adsorption properties and statistical physics modeling. *Chem. Eng. J.* **473**, 145385. https://doi.org/10.1016/J.CEJ.2023.145385 (2023).

91. Sellaoui, L. *et al.* Novel films prepared from spirulina and chitosan for textile pollutant removal: Experiments and theoretical study of adsorption equilibrium via an advanced theoretical approach. *Sep. Purif. Technol.* **329**, 125158. https://doi.org/10.1016/J.SEPPUR.2023.125158 (2024).

92. Kuang, Y., Zhang, X. & Zhou, S. Adsorption of methylene blue in water onto activated carbon by surfactant modification. *Water* **12**, 587. https://doi.org/10.3390/W12020587 (2020).

93. Popek, E. Environmental chemical pollutants. *Sampl. Anal. Environ. Chem. Pollut.* https://doi.org/10.1016/B978-0-12-803202-2.00002-1 (2018).

94. Petrovic, M., Gehringer, P., Eschweiler, H. & Barceló, D. Radiolytic decomposition of multi-class surfactants and their biotransformation products in sewage treatment plant effluents. *Chemosphere.* **66**, 114–122. https://doi.org/10.1016/J.CHEMOSPHERE.2006.05.008 (2007).

95. Zhou, H., Su, Y., Chen, X. & Wan, Y. Separation of acetone, butanol and ethanol (ABE) from dilute aqueous solutions by silicalite-1/PDMS hybrid pervaporation membranes. *Sep. Purif. Technol.* **79**, 375–384. https://doi.org/10.1016/J.SEPPUR.2011.03.026 (2011).

96. Janoš, P. & Šmídová, V. Effects of surfactants on the adsorptive removal of basic dyes from water using an organomineral sorbent—iron humate. *J. Colloid Interface Sci.* **291**, 19–27. https://doi.org/10.1016/J.JCIS.2005.04.065 (2005).

97. Wei, P., Zhang, Y., Huang, Y. & Chen, L. Structural design of SiO2/TiO2 materials and their adsorption-photocatalytic activities and mechanism of treating cyanide wastewater. *J. Mol. Liq.* **377**, 121519 (2023).

98. Halhouli, K. A., Darwish, N. A. & Al-Dhoon, N. M. Effects of pH and inorganic salts on the adsorption of phenol from aqueous systems on activated decolorizing charcoal. *Sep. Sci. Technol.* **30**, 3313–3324 (1995).

99. Bian, Y. *et al.* Effect of inorganic salt ions on the adsorption of quinoline using coal powder. *Water Sci. Technol.* **78**, 496–505. https://doi.org/10.2166/WST.2018.300 (2018).

100. Zhao, X. *et al.* Post-synthesis introduction of dual functional groups in metal–organic framework for enhanced adsorption of moxifloxacin antibiotic. *J. Colloid Interface Sci.* **639**, 59–67 (2023).

101. Zhao, W. *et al.* Rapid adsorption of dyes from aqueous solutions by modified lignin derived superparamagnetic composites. *J. Mol. Struct.* **1261**, 132954. https://doi.org/10.1016/J.MOLSTRUC.2022.132954 (2022).

102. Darul Raiyaan, G., Mohamed Khalith, S., Asrar Sheriff, M. & Arunachalam, K. D. Bio-adsorption of methylene blue dye using chitosan-extracted from Fenneropenaeus indicus shrimp shell waste. *J. Aquac. Mar. Biol.* **10**, 146–150 (2021).

103. Zeybek, N., Büyükkileci, A. O., Güleç, S., Polat, M. & Polat, H. Designing robust xylan/chitosan composite shells around drug-loaded MSNs: Stability in upper GIT and degradation in the colon microbiota. *J. Drug Deliv. Sci. Technol.* **79**, 103983 (2023).

104. Li, H. *et al.* Family 92 carbohydrate-binding modules specific for β-1, 6-glucans increase the thermostability of a bacterial chitinase. *Biochimie.* **212**, 153–160 (2023).

105. Silva, F. R. F. *et al.* Anticoagulant activity, paw edema and pleurisy induced carrageenan: Action of major types of commercial carrageenans. *Carbohydr. Polym.* **79**, 26–33. https://doi.org/10.1016/J.CARBPOL.2009.07.010 (2010).

106. Huang, C. *et al.* Carbon quantum dot decorated hollow In 2 S 3 microspheres with efficient visible-light-driven photocatalytic activities. *RSC Adv.* **6**, 40137–40146. https://doi.org/10.1039/C6RA01348A (2016).

107. Lim, S. H. & Hudson, S. M. Synthesis and antimicrobial activity of a water-soluble chitosan derivative with a fiber-reactive group. *Carbohydr. Res.* **339**, 313–319. https://doi.org/10.1016/J.CARRES.2003.10.024 (2004).

108. Queiroz, M. F., Melo, K. R. T., Sabry, D. A., Sassaki, G. L. & Rocha, H. A. O. Does the use of chitosan contribute to oxalate kidney stone formation?. *Mar. Drugs* **13**, 141–158. https://doi.org/10.3390/MD13010141 (2014).

109. Benamer Oudih, S. *et al.* Chitosan nanoparticles with controlled size and zeta potential. *Polym. Eng. Sci.* **63**, 1011–1021 (2023).

110. Zarandona, I. *et al.* Magnetically responsive chitosan-pectin films incorporating Fe_3O_4 nanoparticles with enhanced antimicrobial activity. *Int. J. Biol. Macromol.* **227**, 1070–1077 (2023).

111. Sakkayawong, N., Thiravetyan, P. & Nakbanpote, W. Adsorption mechanism of synthetic reactive dye wastewater by chitosan. *J. Colloid Interface Sci.* **286**, 36–42. https://doi.org/10.1016/J.JCIS.2005.01.020 (2005).

Competing interests

The authors declare no competing interests.

Additional information

Correspondence and requests for materials should be addressed to M.A.

Reprints and permissions information is available at www.nature.com/reprints.

Publisher's note Springer Nature remains neutral with regard to jurisdictional claims in published maps and institutional affiliations.